ATLAS CONF Note

ATLAS-CONF-2020-009

17th April 2020

Search for trilepton resonances from chargino and neutralino pair production in $\sqrt{s} = 13$ TeV pp collisions with the ATLAS detector

The ATLAS Collaboration

A search is performed for the electroweak pair production of charginos and neutralinos which each decay through an R-parity-violating coupling to a lepton and a W, Z, or Higgs boson. The trilepton invariant mass spectrum is constructed from events with three or more leptons, targeting chargino decays that include an electron or muon and a leptonically-decaying Z boson. The analyzed dataset corresponds to an integrated luminosity of 139 fb^{-1} of proton-proton collision data produced by the Large Hadron Collider at a center-of-mass energy of $\sqrt{s}$ = 13 TeV and collected by the ATLAS experiment between 2015 and 2018. The data are found to be consistent with predictions from the Standard Model. The results are interpreted as limits at 95% confidence level on model-independent cross sections for processes beyond the Standard Model. Limits are also set on the production of charginos and neutralinos for a Minimal Supersymmetric Standard Model with an approximate $B - L$ symmetry. Charginos and neutralinos with masses between 100 GeV and 1050 GeV are excluded for various assumptions on the decay branching fractions into electron, muon, or τ leptons and into W, Z, or Higgs bosons.

ATLAS-CONF-2020-009
17 April 2020

1 Introduction

The extension of the Standard Model (SM) of particle physics with supersymmetry (SUSY) [1–6] can introduce processes that violate baryon number (B) and lepton number (L), for instance proton decay. As such processes have not been observed it is common to introduce an *ad hoc* requirement to conserve R-parity [7], defined as $R = (-1)^{3(B-L)+2s}$, where s is spin. All SM particles have $R = 1$ and their SUSY partners have $R = -1$, and R-parity conservation (RPC) therefore requires the lightest SUSY particle (LSP) to be stable. In RPC scenarios, a stable LSP must necessarily be neutral in electric and color charge to be compatible with astrophysical data [8, 9].

Theories predicting R-parity violation (RPV) [10, 11] are viable if the $B - L$ violating interactions have small couplings and violate only one of B or L at tree level, thus preventing proton decay. The benchmark model for this search is a Minimal Supersymmetric Standard Model (MSSM) [12, 13] extension that adds a gauged $U(1)_{B-L}$ [14–18] to the $SU(3)_{\mathrm{C}} \times SU(2)_{\mathrm{L}} \times U(1)_{\mathrm{Y}}$ of the SM and includes three generations of right-handed neutrino supermultiplets. The third generation right-handed sneutrino has the correct quantum numbers to spontaneously break the $B - L$ symmetry, and its vacuum expectation value (VEV) only introduces L violation at tree level. The size of the RPV coupling is directly related to the right-handed sneutrino VEV, and therefore to the neutrino sector, and is kept small by the lightness of the neutrino masses. The LSP may decay into SM particles through the RPV coupling, which allows the LSP to have electric and color charges.

The $B - L$ RPV model predicts unique signatures [19, 20] that are forbidden under the assumption of R-parity conservation. In a set of simulations [21, 22] where the MSSM parameters were scanned and the resulting LSP was calculated for each simulation, it was seen [23, 24] that two likely LSP candidates with moderate production cross sections at the LHC are the wino-type chargino ($\tilde{\chi}_1^{\pm}$) and wino-type neutralino ($\tilde{\chi}_1^0$), the SUSY partners of the electroweak gauge fields of the W bosons. Both LSP candidates were found to be nearly mass degenerate with one another for all simulations and therefore both primarily decay via RPV couplings [23]. The RPV coupling was found to be large enough such that both the $\tilde{\chi}_1^{\pm}$ and $\tilde{\chi}_1^0$ decay promptly [24], and this search targets prompt decays. The chargino can decay to either a Z boson and a charged lepton ($Z\ell$), a Higgs boson and a charged lepton ($H\ell$), or a W boson and a neutrino ($W\nu$), while the neutralino can decay to either $W\ell$, $Z\nu$, or $H\nu$, as shown in Figure 1. The relative $\tilde{\chi}_1^{\pm}/\tilde{\chi}_1^0$ branching fractions depend on $\tan\beta$, the ratio of the VEV of the two Higgs fields, and the neutrino mass hierarchy. For example, the $\tilde{\chi}_1^{\pm}/\tilde{\chi}_1^0$ branching fraction to electrons is predicted to be small under the normal hierarchy.

This paper presents a search for the pair-production of two charginos ($\tilde{\chi}_1^{\pm}\tilde{\chi}_1^{\mp}$) or a chargino and neutralino ($\tilde{\chi}_1^{\pm}\tilde{\chi}_1^0$). In contrast to RPC searches there is no significant missing transverse momentum from an invisible LSP in the event, and all decay products can be visible in the detector. A resonance search in the trilepton mass ($m_{Z\ell}$) is performed in three signal regions, all of which target events where the decay of at least one $\tilde{\chi}_1^{\pm}$ forms a trilepton resonance. One signal region requires four or more leptons and targets events where the second $\tilde{\chi}_1^{\pm}/\tilde{\chi}_1^0$ decay can be fully reconstructed. A second signal region also requires four or more leptons but targets decays of the second $\tilde{\chi}_1^{\pm}/\tilde{\chi}_1^0$ that include one or more leptons and at least one neutrino. A third signal region requires exactly three leptons, targeting decays of the second $\tilde{\chi}_1^{\pm}/\tilde{\chi}_1^0$ that include no leptons.

Several SM processes with similar final-state particles can contribute to the signal regions, with the largest contributions from the WZ, ZZ, and $t\bar{t}Z$ processes. The expected yields of these processes are estimated using Monte Carlo simulation that is normalized to data in three high-statistics control regions. Additional

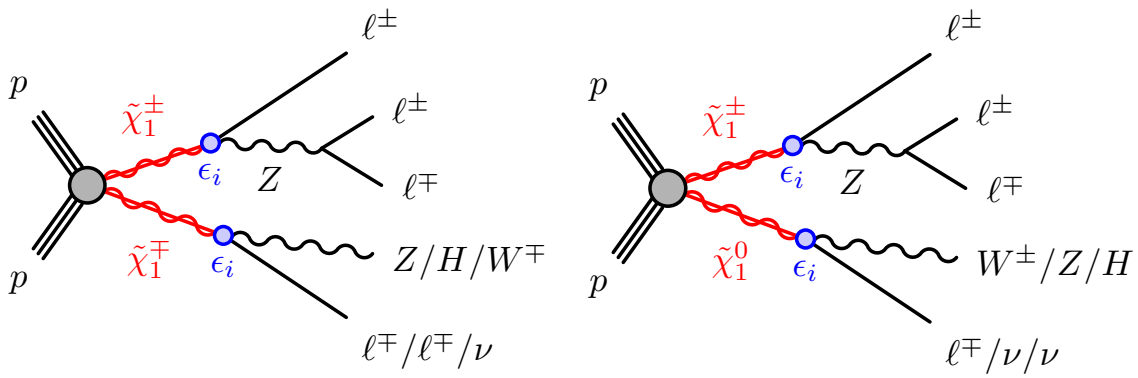

Figure 1: Diagrams of (left) $\tilde{\chi}_1^{\pm}\tilde{\chi}_1^{\mp}$ and (right) $\tilde{\chi}_1^{\pm}\tilde{\chi}_1^{0}$ production with at least one $\tilde{\chi}_1^{\pm} \to Z\ell \to \ell\ell\ell$ decay. The R-parity violating coupling ϵ_i allows for prompt $\tilde{\chi}_1^{\pm}$ decays to $Z\ell$, $H\ell$, or $W\nu$ and prompt $\tilde{\chi}_1^{0}$ decays to $W\ell$, $Z\nu$, or $H\nu$.

event selections are applied to reject events from SM processes in the signal regions while maintaining a high selection efficiency of the target $\tilde{\chi}_1^{\pm}\tilde{\chi}_1^{\mp}$ and $\tilde{\chi}_1^{\pm}\tilde{\chi}_1^{0}$ models.

A scan over the possible $\tilde{\chi}_1^{\pm}/\tilde{\chi}_1^{0}$ branching fractions to both bosons and leptons is performed when setting model-specific limits. Model-independent limits are also explored in narrow slices of the $m_{Z\ell}$ spectrum, with no assumptions made on the $\tilde{\chi}_1^{\pm}/\tilde{\chi}_1^{0}$ branching fractions or decay kinematics of a generic beyond-the-SM process.

Previous searches for the pair production of wino-type charginos and neutralinos in R-parity conserving models that targeted final states with three or more leptons via W and Z boson decays found no significant excess in data over background expectations, with the ATLAS [25, 26] and CMS [27, 28] collaborations setting limits on wino masses of up to 580 GeV and 650 GeV, respectively. Searches have also been performed for trilepton resonances from heavy leptons in type-III seesaw scenarios by the ATLAS [29, 30] and CMS [31] collaborations, but none have attempted to fully reconstruct both decay chains in a pair-produced event. A previous search by ATLAS [32] for the $B-L$ RPV model targeted by this analysis focused on the pair-production of top squarks [33].

A brief overview of the ATLAS detector is given in Section 2, and a description of the dataset and the Monte Carlo simulation is presented in Section 3. Details of the reconstruction of the events used in the search are presented in Section 4, and the design of signal regions sensitive to the $B-L$ RPV model is discussed in Section 5. The description of the SM backgrounds and the strategy for their estimation is given in Section 6, followed by an explanation of the systematic uncertainties in Section 7. The results of the search and their interpretation for various $B-L$ RPV model scenarios are presented in Section 8, and the conclusion given in Section 9.

2 ATLAS detector

The ATLAS detector [34] is a multipurpose particle detector with a nearly 4π coverage in solid angle[1]. It is composed of an inner tracking system covering the pseudorapidity region $|\eta| < 2.5$, sampling electromagnetic and hadronic calorimeters covering $|\eta| < 4.9$, and a muon spectrometer covering $|\eta| < 2.7$. The inner detector (ID) reconstructs tracks from charged particles using silicon pixel, silicon microstrip, and transition radiation tracking detectors. The innermost layer of the silicon pixel tracker, the insertable B-layer [35, 36], was installed prior to 2015 at an average radial distance of 3.3 cm from the beamline to improve track reconstruction and the identification of jets initiated by heavy-flavor hadrons. The ID is surrounded by a thin superconducting solenoid providing a 2 T axial magnetic field, facilitating the measurement of charged-particle momenta.

Beyond the solenoid is a high-granularity lead/liquid-argon (LAr) electromagnetic sampling calorimeter covering $|\eta| < 3.2$. Outside the electromagnetic calorimeter are two hadronic calorimeters; a steel/scintillator-tile sampling calorimeter covering $|\eta| < 1.7$ and a copper/LAr endcap calorimeter covering $1.7 < |\eta| < 3.2$. The most forward region of $3.1 < |\eta| < 4.9$ is covered by copper/LAr and tungsten/LAr calorimeters optimized for electromagnetic and hadronic measurements, respectively.

The muon spectrometer (MS) surrounds the calorimeters, identifying and measuring muon tracks through three layers of precision tracking and triggering chambers. The MS is interleaved with a system of three superconducting air-core toroidal magnets with eight coils each, with a field integral between 2.0 T m and 6.0 T m across most of the detector.

The ATLAS trigger system consists of a hardware-based Level 1 (L1) trigger followed by a software-based high-level trigger (HLT) [37]. The L1 and HLT trigger systems are designed to accept events at average rates of 100 kHz and 1 kHz, respectively. Candidate electrons within $|\eta| < 2.5$ are identified by the L1 trigger as compact electromagnetic energy deposits in the electromagnetic calorimeter, and by the HLT using additional fast track reconstruction [38]. Candidate muons within $|\eta| < 2.7$ are identified by the L1 trigger through a coincidence of MS trigger chamber layers and further selected by the HLT using fast reconstruction algorithms with input from the ID and MS.

3 Data and Monte Carlo simulation

The analysis is performed on pp collision data collected by the ATLAS experiment between the years 2015 and 2018. The dataset corresponds to a total integrated luminosity of 139 fb^{-1} after imposing data quality requirements [39]. In this dataset there are, on average, approximately 34 simultaneous pp collisions in each LHC bunch crossing.

Monte Carlo (MC) simulation is used to model the expected contributions of various SM processes and the $\tilde{\chi}_1^{\pm}\tilde{\chi}_1^{\mp}$ and $\tilde{\chi}_1^{\pm}\tilde{\chi}_1^{0}$ signal processes targeted by the search. It is used to define and optimize the event selection criteria and to estimate systematic uncertainties of the event yield predictions. The generators and parameters used in the MC simulation samples are given below and summarized in Table 1. The

[1] ATLAS uses a right-handed coordinate system with its origin at the nominal interaction point (IP) in the center of the detector and the z-axis along the beam pipe. The x-axis points from the IP to the center of the LHC ring, and the y-axis points upwards. Cylindrical coordinates (r, ϕ) are used in the transverse plane, ϕ being the azimuthal angle around the z-axis. The pseudorapidity is defined in terms of the polar angle θ as $\eta = -\ln\tan(\theta/2)$, and the rapidity y is defined as $y = (1/2)\ln[(E + p_z)/(E - p_z)]$, where E is energy and p_z is longitudinal momentum. Angular distance is measured in units of $\Delta R \equiv \sqrt{(\Delta\eta)^2 + (\Delta\phi)^2}$

expected yields of SM processes are taken directly from MC simulation except for the dominant WZ, ZZ, and $t\bar{t}Z$ backgrounds, which are estimated from MC simulation that is normalized to data in dedicated control regions, as described in Section 6.1. The contribution from events with one or more misidentified or nonprompt (*fake*) leptons is separately predicted using a data-driven method described in Section 6.2.

Diboson, triboson, and Z+jets samples [40, 41] were simulated using the SHERPA 2.2 [42] generator. Triboson and most diboson processes were simulated with SHERPA 2.2.2 while Z+jets and semileptonically decaying diboson processes were simulated with SHERPA 2.2.1. The matrix element calculations were matched to the parton shower (PS) simulation using Catani–Seymour dipole factorization [43, 44]. The matching was performed separately for different jet multiplicities and merged into an inclusive sample using an improved CKKW matching procedure [45, 46] extended to next-to-leading-order (NLO) accuracy using the MEPS@NLO prescription [45–48]. The virtual QCD correction for matrix elements at NLO accuracy was provided by the OPENLOOPS library [49, 50]. The NNPDF3.0NNLO [51] set of parton distribution functions (PDFs) was used together with a dedicated set of tuned PS parameters (tune) developed by the SHERPA authors [44].

The Z+jets (diboson) samples were calculated for up to two (one) additional partons at NLO and up to four (three) additional partons at leading order (LO), and the triboson samples were calculated at NLO for the inclusive processes and at LO for up to two additional parton emissions. Diboson samples include loop-induced and electroweak production. The diboson and triboson samples do not include Higgs boson contributions. The cross sections calculated by the event generators are used for all samples except for Z+jets, which was normalized to a next-to-next-to-leading order (NNLO) cross section prediction [52].

Samples of $t\bar{t}$ [53], $t\bar{t}H$ [54], and tW [55] processes were simulated at NLO using the POWHEGBOX [56–58] v2 generator and the NNPDF3.0NLO PDF set. The matrix element calculations were interfaced with PYTHIA8.230 [59] for the PS using the A14 tune [60] and the NNPDF2.3LO PDF set [61]. The h_{damp} parameter[2] was set to a factor of 1.5 larger than the top quark mass [62]. The $t\bar{t}$ inclusive production cross section was corrected to the theory prediction calculated at NNLO in QCD and including the resummation of next-to-next-to-leading logarithmic (NNLL) soft-gluon terms calculated with TOP++2.0 [63]. The tW inclusive production cross section was corrected to the theory prediction at NLO in QCD with NNLL corrections to the soft-gluon terms [64, 65]. Both samples were generated in the five-flavor scheme, setting all quark masses to zero except for the top quark. The diagram removal strategy [66] was employed in the tW sample to remove the interference with $t\bar{t}$ production [62].

The production of other top quark processes was simulated with the MADGRAPH5_AMC@NLO v2 [67] generator at either NLO with the NNPDF3.0NLO PDF set or at LO using the NNPDF2.3LO PDF set. They were interfaced with PYTHIA8 using the A14 tune and the NNPDF2.3LO PDF set. Generator versions MADGRAPH5_AMC@NLO v2.3 and PYTHIA8.212 were used for tZ, tWZ, $t\bar{t}Z$, $t\bar{t}W$, and $t\bar{t}WZ$ processes, while versions MADGRAPH5_AMC@NLO v2.2 and PYTHIA8.186 were used for $t\bar{t}\gamma$, $t\bar{t}WW$, and 4-top processes. These top quark processes were generated at LO with the exception of $t\bar{t}Z$, $t\bar{t}W$, and tWZ which were generated at NLO.

Higgs boson production via gluon-gluon fusion (ggF) was simulated at NNLO accuracy in QCD using the POWHEGBOX v2 NNLOPS program [68] and interfaced with PYTHIA 8.212 using the `AZNLO` tune [69] and PDF4LHC15 NNLO PDF set [70]. The MC prediction was normalized to the next-to-next-to-next-to-leading order (NNNLO) cross section in QCD plus electroweak corrections at NLO [71, 72].

[2] The h_{damp} parameter controls the transverse momentum p_{T} of the first additional emission beyond the leading-order Feynman diagram in the PS and therefore regulates the high-p_{T} emission against which the $t\bar{t}$ system recoils.

Higgs boson production via vector-boson fusion (VBF) and Higgs boson production in association with a W or Z boson (VH) were generated using PowhegBox v2 and interfaced with Pythia 8.212 using the AZNLO tune and CTEQ6L1 [73] PDF set. The Powheg predictions are accurate to NLO and were tuned to match calculations including effects due to finite heavy-quark masses and soft-gluon resummations up to NNLL. The MC predictions were normalized to NNLO QCD cross section calculations with NLO electroweak corrections [74–77].

The $B-L$ RPV $\tilde{\chi}_1^{\pm}\tilde{\chi}_1^{\mp}$ and $\tilde{\chi}_1^{\pm}\tilde{\chi}_1^{0}$ signal samples were produced using MadGraph5_aMC@NLO v2.6 and the NNPDF2.3LO PDF set with up to two additional partons calculated at LO and interfaced with Pythia8.230 using the A14 tune and NNPDF2.3LO PDF set. The scale parameter for jet–parton CKKW-L matching was set to a quarter of the $\tilde{\chi}_1^{\pm}/\tilde{\chi}_1^{0}$ mass. Samples were generated at masses between 100 GeV and 1500 GeV in steps of 50 GeV. Signals with masses below 100 GeV were not explored as they have been excluded by previous three-lepton searches for charginos and neutralinos [25–31].

Signal events were generated with equal $\tilde{\chi}_1^{\pm}/\tilde{\chi}_1^{0}$ branching fractions to bosons (W, Z, and Higgs bosons where kinematically accessible) and leptons (e, μ, and τ). In the analysis, the simulated events are reweighted according to their generated decays when exploring different $\tilde{\chi}_1^{\pm}/\tilde{\chi}_1^{0}$ branching fraction assumptions. When reweighting, the branching fractions of $\tilde{\chi}_1^{\pm}$ and $\tilde{\chi}_1^{0}$ are assumed to be fully correlated.

Generated signal events were required to have at least three leptons, two of which were associated with a Z boson. Hadronically-decaying τ-leptons were not considered by this three-lepton requirement for the $\tilde{\chi}_1^{\pm}\tilde{\chi}_1^{0}$ events. The $\tilde{\chi}_1^{\pm}$ were also required to decay via a Z boson in the $\tilde{\chi}_1^{\pm}\tilde{\chi}_1^{0}$ events to improve the statistics of events with a trilepton resonance. The inclusive production cross sections were calculated assuming mass-degenerate, wino-like $\tilde{\chi}_1^{\pm}$ and $\tilde{\chi}_1^{0}$, as predicted by the $B-L$ RPV model [23], and were calculated at NLO in QCD with next-to-leading-logarithmic (NLL) corrections to the soft-gluon terms. [78–82]. The cross sections and their uncertainties were derived from an envelope of cross section predictions using different PDF sets and factorization and renormalization scales [83]. The cross sections for $\tilde{\chi}_1^{\pm}\tilde{\chi}_1^{\mp}$ ($\tilde{\chi}_1^{\pm}\tilde{\chi}_1^{0}$) production at a center-of-mass energy of $\sqrt{s} = 13$ TeV range from 11.6 ± 0.5 (22.7 ± 1.0) pb for masses of 100 GeV to 0.040 ± 0.006 (0.080 ± 0.013) fb for masses of 1500 GeV.

The modeling of c- and b-hadron decays in samples generated with Powheg-Box or MadGraph5_aMC@NLO was performed with EvtGen 1.2.0 [84]. Events from all generators were propagated through a full simulation of the ATLAS detector [85] using Geant4 [86] to model the interactions of particles with the detector. A parametrized simulation of the ATLAS calorimeter called Atlfast-II [85] was used for faster detector simulation of signal, tW, and $t\bar{t}H$ processes and was found to be in agreement with the full simulation. The effect of multiple interactions in the same and neighboring bunch crossings (pileup) was modeled by overlaying simulated minimum-bias events onto each hard-scattering event. The minimum-bias events were generated with Pythia8.210 using the A3 tune [87] and NNPDF2.3LO PDF set.

4 Event reconstruction

The data events used in the analysis were recorded during stable beam conditions at the LHC and were required to pass data quality criteria. Data events were collected with triggers requiring at least a single electron or a single muon reconstructed by the trigger system, with various lepton p_{T} thresholds depending upon the relative quality (including isolation) of the trigger-level leptons [37]. In the analysis, tighter quality and p_{T} requirements are applied to the fully reconstructed signal leptons, as described below, to ensure the event selection is free from bias in the trigger reconstruction. Each event is required to have

Table 1: Details of the Monte Carlo simulation for each physics process, including the event generator used for matrix element calculation, the generator used for the PS and hadronization, the PS parameter tunes, and the order in α_S of the production cross section calculations.

Process	Event generator	PS and hadronization	PS tune	Cross section (in QCD)
Diboson, Triboson, (Z+jets)	Sherpa 2.2	Sherpa 2.2	Default	NLO (NNLO)
$t\bar{t}W$, $t\bar{t}Z$, (Other top)	MadGraph5_aMC@NLO 2	Pythia 8	A14	NLO (LO)
$t\bar{t}$, (tW), [$t\bar{t}H$]	Powheg-Box v2	Pythia 8	A14	NNLO+NNLL (NLO+NNLL) [NLO]
Higgs: ggF, (VBF, VH)	Powheg-Box v2	Pythia 8	AZNLO	NNNLO (NNLO+NNLL)
$\tilde{\chi}_1^{\pm}\tilde{\chi}_1^{\mp}$, $\tilde{\chi}_1^{\pm}\tilde{\chi}_1^{0}$	MadGraph 2.6	Pythia 8	A14	NLO+NLL

at least one electron (muon) in the event that activated the trigger and which has a fully-calibrated p_{T} above 27, 61, or 141 GeV (27.3 or 52.5 GeV), with larger p_{T} requirements corresponding to reduced lepton quality requirements of the trigger. For the 2015 data, the p_{T} requirement of the analysis for the loosest quality electron trigger is lowered to 121 GeV. The single-lepton triggers are found to be more than 90% efficient for the signal model with mass of 100 GeV and more than 99% efficient for signal models of mass 300 GeV or higher.

Both data and MC events are required to have at least one reconstructed vertex that is associated with two or more tracks of transverse momentum $p_{\mathrm{T}} > 500$ MeV. The primary vertex of each event is selected as the vertex with the largest Σp_{T}^2 of associated tracks [88].

The primary objects considered by this analysis are electrons, muons, and jets. Electron candidates are reconstructed from three-dimensional energy clusters in the electromagnetic calorimeter which are matched to an ID track, and they are calibrated *in situ* using $Z \to ee$ decays [89]. Muon candidates in the detector are reconstructed from either a combined fit of tracks formed in the MS and ID or from track segments in the MS matched to an ID track, and they are calibrated *in situ* using $Z \to \mu\mu$ and $J/\psi \to \mu\mu$ decays [90]. Jet candidates are reconstructed from three-dimensional energy clusters formed using both the electromagnetic and hadronic calorimeters [91] and which are grouped using the anti-k_t algorithm [92, 93] with a radius parameter $R = 0.4$. The jet energy scale (JES) and resolution (JER) are first corrected to particle level using MC simulation and then calibrated *in situ* through Z+jets, γ+jets, and multijet measurements [94].

Two levels of selection criteria are defined for leptons and jets; the looser "baseline" criteria and the tighter "signal" criteria. Baseline objects are used for resolving ambiguities between overlapping objects, calculating the missing transverse momentum ($\mathbf{p}_{\mathrm{T}}^{\mathrm{miss}}$) of an event, and as inputs to the data-driven estimation of *fake*-lepton events. Baseline electrons are required to pass the "loose and B-layer likelihood" quality criteria [89], satisfy $p_{\mathrm{T}} > 10$ GeV, and be within the ID acceptance ($|\eta| < 2.47$) and outside the crack region of the electromagnetic calorimeter ($1.37 < |\eta| < 1.52$). Baseline muons are required to pass the "medium" quality criteria [90], satisfy $p_{\mathrm{T}} > 10$ GeV, and fall within the MS acceptance ($|\eta| < 2.7$). Each baseline electron and muon is also required to have a trajectory consistent with the primary vertex to suppress pileup. For this purpose, the transverse impact parameter (d_0) of a lepton is defined as the distance in the transverse plane between the beam-line and the closest point of the associated ID track. The longitudinal impact parameter (z_0) then corresponds to the z-coordinate distance between that point and the primary vertex. A selection of $|z_0 \sin\theta| < 0.5$ mm is required for each lepton to ensure it is compatible with the primary vertex.

Baseline jets are required to satisfy $p_{\mathrm{T}} > 20$ GeV and fall within the full calorimeter acceptance ($|\eta| < 4.5$). The identification of baseline jets containing b-hadrons (b-jets) is performed using a

multivariate discriminant built using information from track impact parameters, the presence of displaced secondary vertices, and the reconstructed flight paths of b- and c-hadrons inside the jet [95]. The identification criteria are tuned to an average identification efficiency of 85% as obtained for b-jets in simulated $t\bar{t}$ events, corresponding to rejection factors of 25, 2.7, and 6.1 for jets originating from light-quarks and gluons, c-quarks, and τ-leptons, respectively.

While photons are not used directly in the analysis, baseline photons are defined for use in the calculation of $\mathbf{p}_{\mathrm{T}}^{\mathrm{miss}}$. Baseline photons are required to pass the "tight" quality criteria [89], satisfy $p_{\mathrm{T}} > 25$ GeV, and fall within the ID acceptance ($|\eta| < 2.37$) and outside the crack region ($1.37 < |\eta| < 1.52$).

To prevent the reconstruction of a single particle as multiple objects, an overlap removal procedure is performed with baseline leptons and jets. First, any electron that shares a track with a muon in the ID is removed, as the track is consistent with track segments in the MS. Next, jets are removed if they are within $\Delta R = 0.2$ of a lepton and are either not b-tagged or satisfy $p_{\mathrm{T}} > 100$ GeV, as they are consistent with the energy deposited by an electron shower or muon bremsstrahlung. For the overlap of a jet with a nearby muon, the jet is discarded only if it is associated with fewer than three tracks of $p_{\mathrm{T}} \geq 500$ MeV. Finally, electrons and muons within $\Delta R = 0.4$ of any remaining jets are discarded to reject *fake* leptons originating from hadron decays. In the overlap removal procedure the calculation of ΔR uses rapidity instead of η to ensure the distance measurement is Lorentz invariant for jets with non-negligible masses.

The $\mathbf{p}_{\mathrm{T}}^{\mathrm{miss}}$ of each event, with magnitude $E_{\mathrm{T}}^{\mathrm{miss}}$, is defined as the negative vector sum of the transverse momenta of all identified baseline objects (electrons, muons, jets, and photons) and an additional soft term [96]. The soft term is constructed from all tracks associated with the primary vertex that are not associated with any baseline object. The $\mathbf{p}_{\mathrm{T}}^{\mathrm{miss}}$ is therefore adjusted to include the full calibration of the reconstructed baseline objects while minimizing any pileup dependence in the soft term.

Tighter "signal" criteria are applied to the final leptons and jets considered by the analysis to ensure a high selection purity and accurate p_{T} measurement. Any event with a baseline lepton that fails the signal criteria is rejected to reduce the contamination from *fake*-lepton events. Signal leptons are required to have $p_{\mathrm{T}} > 12$ GeV and electrons must pass the "medium" quality criteria [89]. At least one signal lepton in the event must pass the larger p_{T} requirement of an associated trigger. The track associated with each signal electron or muon must pass a requirement on d_0 and its uncertainty σ_{d_0} such that $|d_0/\sigma_{d_0}| < 5$ (3) for electrons (muons), ensuring the selection of leptons with prompt, well-reconstructed tracks. Finally, signal leptons must be sufficiently isolated from additional detector activity by passing a p_{T}-dependent "tight" requirement on both calorimeter-based and track-based isolation variables. The calorimeter-based isolation is defined within a cone of size $\Delta R = 0.2$ around the lepton, and the amount of nonassociated calorimeter transverse energy within the cone must be below 6% (15%) of the electron (muon) p_{T}. The track-based isolation cone size is $\Delta R = 0.2$ for low-p_{T} electrons and decreases linearly with p_{T} above 50 GeV as the electron's shower becomes more collimated. For muons, the size of the track-isolation cone is $\Delta R = 0.3$ for muons with $p_{\mathrm{T}} \leq 33$ GeV and decreases linearly with p_{T} to $\Delta R = 0.2$ at $p_{\mathrm{T}} = 50$ GeV, improving the selection efficiency for higher-p_{T} muons. The track-based isolation only considers nonassociated tracks that are consistent with the primary vertex, and the scalar sum of track p_{T} ($p_{\mathrm{T}}^{\mathrm{iso}}$) is required to be below 6% (4%) of the electron (muon) p_{T}. The lepton $p_{\mathrm{T}}^{\mathrm{cone}}$ is then defined as the scalar sum of the lepton p_{T} and $p_{\mathrm{T}}^{\mathrm{iso}}$, and is useful in parametrizing the behavior of *fake* leptons.

Signal jets are required to have $|\eta| < 2.8$, and events are rejected if they contain a jet that fails to meet the "loose" quality criteria [97], reducing contamination from electronic noise bursts and noncollision backgrounds. To suppress jets originating from pileup, jets with $p_{\mathrm{T}} < 120$ GeV and within the ID acceptance ($|\eta| < 2.5$) are required to pass the "medium" working point of the track-based jet vertex

tagger [98, 99]. All MC simulation samples are corrected to account for small differences with data in signal lepton identification, reconstruction, isolation and triggering efficiencies, as well as in signal jet pileup rejection and flavor identification efficiencies.

5 Search strategy

The $B-L$ RPV model allows for many different decay modes of $\tilde{\chi}_1^{\pm}/\tilde{\chi}_1^0$ and therefore many possible final states. A decay that would be particularly discernible in a search is $\tilde{\chi}_1^{\pm} \to Z\ell \to \ell\ell\ell$ because of the large number of leptons produced from a single resonance. The invariant mass distribution of the trilepton resonance ($m_{Z\ell}$) is narrow due to the excellent momentum resolution of reconstructed electrons and muons. No SM process naturally produces a three-lepton resonance, leading to a smooth, combinatorial background distribution in which a resonance would be distinguishable.

Three orthogonal signal regions (SRs) are developed in Section 5.1 to select $\tilde{\chi}_1^{\pm}\tilde{\chi}_1^{\mp}$ and $\tilde{\chi}_1^{\pm}\tilde{\chi}_1^0$ events with at least one $\tilde{\chi}_1^{\pm} \to Z\ell \to \ell\ell\ell$ decay. Each SR targets different decay scenarios of the second $\tilde{\chi}_1^{\pm}/\tilde{\chi}_1^0$ through requirements on the number of leptons and reconstructed W, Z, or Higgs bosons. The SRs utilize event-wide information to reduce combinatorial backgrounds, as described in Section 5.3.

5.1 Signal regions targeting trilepton decays

Each SR requires at least three signal leptons, two of which are identified as candidates of a Z boson decay if they have the same flavor and opposite sign of their electric charge (SFOS) and have an invariant mass $m_{\ell\ell}$ within 10 GeV of the Z boson mass. If there is more than one SFOS pair, the pair with $m_{\ell\ell}$ closest to the Z mass is chosen. The $m_{Z\ell}$ of the $\tilde{\chi}_1^{\pm}$ is then reconstructed from the chosen SFOS pair and a third lepton. Deviations of $m_{\ell\ell}$ from the expected Z boson mass of 91.2 GeV can occur due to the imperfect energy reconstruction of leptons, particularly at high p_{T}. The $m_{Z\ell}$ resolution is therefore improved by shifting the value of $m_{Z\ell}$ by an amount equal to $(91.2 - m_{\ell\ell})$ GeV.

Events are separated into the three SRs according to the number of leptons and the presence of a second reconstructed Z, W, or Higgs boson from the second $\tilde{\chi}_1^{\pm}/\tilde{\chi}_1^0$ decay. The SRFR region targets events where

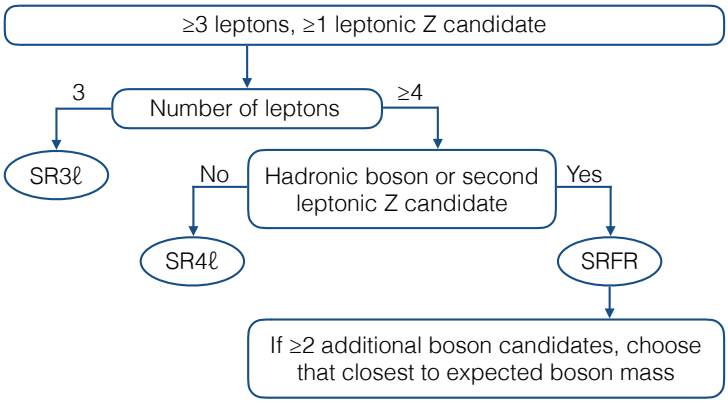

Figure 2: Schematic flow chart describing the assignment of an event into a given signal region.

all decay products are visible and "fully reconstructed". The SR4ℓ region targets events with four or more leptons and possible $E_{\mathrm{T}}^{\mathrm{miss}}$ while the SR3ℓ region targets events with only three visible leptons and substantial $E_{\mathrm{T}}^{\mathrm{miss}}$, with at least one neutrino coming from the decay of the second $\tilde{\chi}_1^{\pm}/\tilde{\chi}_1^0$. The choice of SR for an event is described below and summarized in Figure 2, and all additional selections are applied after the SR is decided.

To target fully-visible events, SRFR requires a fourth lepton and a second reconstructed Z, W, or Higgs boson. Pairs of jets are considered for the second boson if their invariant mass m_{jj} is consistent with that of a W or Z boson, with $71.2 < m_{jj} < 111.2$ GeV. If at least one of the jets is a b-jet, the m_{jj} requirement is loosened to $71.2 < m_{jj} < 150$ GeV to allow for Higgs boson decays. Additional SFOS lepton pairs are also considered if their invariant mass is consistent with the Z boson mass, such that $81.2 < m_{\ell\ell} < 101.2$ GeV. If there are multiple candidates for the second boson, the pairing selected is that with invariant mass closest to the Z boson mass, or closest to the Higgs boson mass for pairs that include at least one b-jet.

The SR4ℓ region targets events in which the decay of the second $\tilde{\chi}_1^{\pm}/\tilde{\chi}_1^0$ includes one or more leptons but is not fully reconstructed due to the presence of neutrinos. Events with four or more leptons that fail all SRFR requirements are selected by SR4ℓ. The SR3ℓ region targets decays of the second $\tilde{\chi}_1^{\pm}/\tilde{\chi}_1^0$ that include no leptons, requiring exactly three leptons in the event. While each region targets specific $\tilde{\chi}_1^{\pm}/\tilde{\chi}_1^0$ decay chains, events in which one or more leptons fall outside the detector acceptance or are not reconstructed may still be selected by other regions. For the signal sample with a mass of 500 GeV and democratic $\tilde{\chi}_1^{\pm}/\tilde{\chi}_1^0$ branching fractions, the SRFR, SR4ℓ, and SR3ℓ regions have a selection efficiency of 3%, 4%, and 5%, respectively.

Within each SR the search is performed in the $m_{Z\ell}$ spectrum to maximize the discovery sensitivity to a resonance. The binning of the $m_{Z\ell}$ observable was optimized using $\tilde{\chi}_1^{\pm}\tilde{\chi}_1^{\mp}$ and $\tilde{\chi}_1^{\pm}\tilde{\chi}_1^0$ signal samples given the predicted background expectation, with lower edges at

$$m_{Z\ell} = 90, 110, 130, 150, 170, 190, 210, 230, 250, 270, 300, 330, 360, 400, 440, \text{ and } 580 \text{ GeV}.$$

The last bin has no upper edge and includes all events with $m_{Z\ell} > 580$ GeV. The same binning is used for all three SRs, facilitating the discovery of a trilepton resonance that would contribute to all SRs.

5.2 Assignment of direct leptons to $\tilde{\chi}_1^{\pm}/\tilde{\chi}_1^0$ decays

The presence of one or more additional leptons from the second $\tilde{\chi}_1^{\pm}/\tilde{\chi}_1^0$ decay introduces ambiguity in the assignment of a lepton and boson produced directly from a $\tilde{\chi}_1^{\pm}/\tilde{\chi}_1^0$ decay. A matching procedure is implemented to identify the "direct" leptons in an event which come directly from the $\tilde{\chi}_1^{\pm}/\tilde{\chi}_1^0$ decays, rather than from the subsequent decay of a boson, and to assign them to each $\tilde{\chi}_1^{\pm}/\tilde{\chi}_1^0$. The procedure optimizes the sensitivity to signals of various masses by maintaining a high efficiency for the correct assignments while reducing the contamination from SM processes. In SRFR, both the trilepton decay and the fully-visible decay of the second $\tilde{\chi}_1^{\pm}/\tilde{\chi}_1^0$, with reconstructed mass $m_{\tilde{\chi},2}$, are chosen as the groupings that minimize the mass asymmetry between the mass-degenerate $\tilde{\chi}_1^{\pm}\tilde{\chi}_1^{\mp}$ or $\tilde{\chi}_1^{\pm}\tilde{\chi}_1^0$ pair, where $m_{Z\ell}^{\mathrm{asym}}$ is defined as

$$m_{Z\ell}^{\mathrm{asym}} = \frac{|m_{Z\ell} - m_{\tilde{\chi},2}|}{m_{Z\ell} + m_{\tilde{\chi},2}}. \tag{1}$$

The matching efficiency for the signal samples is 60% at 100 GeV and 80% or more for masses of 200 GeV and larger.

The matching procedure for a direct lepton to the Z candidate for all other analysis regions with four or more leptons is developed to optimize the sensitivity of the SR4ℓ region. Two methods are implemented, and the choice of method exploits the correlation between the true mass of the $\tilde{\chi}_1^\pm/\tilde{\chi}_1^0$ and L_T, the scalar sum of the p_T of all leptons in the event. A method targeting low-mass signals is used when $L_\mathrm{T} < 550$ GeV and a method targeting high-mass signals is used when $L_\mathrm{T} \geq 550$ GeV. For low-mass signals, the $\tilde{\chi}_1^\pm/\tilde{\chi}_1^0$ can often be produced with a sufficiently large momentum such that the decay products are near to one another, and the lepton that is closest in angular distance ΔR to the reconstructed Z boson is chosen. For high-mass signals, the $\tilde{\chi}_1^\pm/\tilde{\chi}_1^0$ decay products are often produced at a wide angle in the detector, and mispairings will produce a $m_{Z\ell}$ that is smaller than the $\tilde{\chi}_1^\pm/\tilde{\chi}_1^0$ mass. Therefore, the lepton which maximizes the reconstructed $m_{Z\ell}$ is chosen. The matching efficiency of this procedure for signal samples is 90% at 100 GeV, 30% at 300 GeV, and 70% at 700 GeV. While a low matching efficiency is seen at 300 GeV due to the use of ΔR matching when the $m_{Z\ell}$ maximization would be preferred, the overall analysis sensitivity is improved by avoiding the $m_{Z\ell}$ maximization of low L_T backgrounds.

As noted in Section 1, the preferred flavor of the direct lepton(s) is related to the neutrino mass hierarchy. The sensitivity to $\tilde{\chi}_1^\pm\tilde{\chi}_1^\mp$ and $\tilde{\chi}_1^\pm\tilde{\chi}_1^0$ events may therefore be improved by imposing constraints on the flavor of the direct lepton(s), targeting the favored signal decays while rejecting additional SM backgrounds. Two additional sets of SRs are developed that are each identical to the nominal set of three SRs except that they require the direct lepton(s) to be either electron (SRFR$_e$, SR4ℓ_e, SR3ℓ_e) or muon (SRFR$_\mu$, SR4ℓ_μ, SR3ℓ_μ). These additional "e" and "μ" channels are used separately from the "inclusive" channel and from one another, and are only used when targeting signal models with high $\tilde{\chi}_1^\pm/\tilde{\chi}_1^0$ branching fractions to either electrons or muons, as discussed in Section 8.2.

5.3 Rejecting combinatorial Standard Model backgrounds

The composition and kinematics of the final-state particles that are produced from the decay chains of the $\tilde{\chi}_1^\pm\tilde{\chi}_1^\mp$ or $\tilde{\chi}_1^\pm\tilde{\chi}_1^0$ processes can be combinatorially reproduced by certain SM processes. The ZZ process has a significant contribution to SRFR and SR4ℓ when both Z bosons decay leptonically. Events from the ZZ process are rejected if they have exactly four leptons that form two SFOS pairs and the mass $m_{\ell\ell,2}$ of the second pair, the pair not selected for the primary $\tilde{\chi}_1^\pm$ candidate, is within 20 GeV of the Z boson mass. In SR4ℓ, which targets decay chains of the second $\tilde{\chi}_1^\pm/\tilde{\chi}_1^0$ with at least one neutrino, the ZZ contribution is further reduced by requiring $E_\mathrm{T}^\mathrm{miss} > 80$ GeV in events with a second same-flavor lepton pair.

The SM $t\bar{t}Z$ process can also contribute significantly in the SRs, and is identifiable by the presence of two b-jets from the two top quark decays. Signal events that include a Higgs boson decay may also include two b-jets, but the b-jets will often by collimated due to the boost of the Higgs boson. Therefore, an additional selection is applied in all SRs that requires the leading two b-jets, if they exist, to satisfy $\Delta R(b_1, b_2) < 1.5$.

The ZZ, $t\bar{t}Z$, and other SM backgrounds can be further reduced in SRFR by taking advantage of the fully-visible decay of the second $\tilde{\chi}_1^\pm/\tilde{\chi}_1^0$. As the $\tilde{\chi}_1^\pm$ and $\tilde{\chi}_1^0$ are expected to be mass-degenerate, the $m_{Z\ell}^\mathrm{asym}$ (Equation 1) between the $\tilde{\chi}_1^\pm\tilde{\chi}_1^\mp$ or $\tilde{\chi}_1^\pm\tilde{\chi}_1^0$ pair is expected to be small. A requirement of $m_{Z\ell}^\mathrm{asym} < 0.1$ in SRFR is effective at rejecting combinatorial backgrounds for which $m_{Z\ell}^\mathrm{asym}$ is more evenly distributed.

A significant amount of $E_\mathrm{T}^\mathrm{miss}$ is expected in SR3ℓ as the second $\tilde{\chi}_1^\pm/\tilde{\chi}_1^0$ decays directly into a neutrino and a boson, whose decay may also produce neutrinos. A requirement of $E_\mathrm{T}^\mathrm{miss} > 150$ GeV reduces contamination from SM processes with no neutrinos, particularly Z+jets events that include a *fake* lepton.

The SM WZ process with fully-leptonic decays is also a significant contributor to SR3ℓ, and contains a single neutrino from the W decay. The measured $E_{\mathrm{T}}^{\mathrm{miss}}$ is therefore representative of the p_{T} of the neutrino, and the transverse mass m_{T} of the W boson can be reconstructed from the p_{T} of the lepton and the azimuthal separation $\Delta\phi$ between the lepton and $\mathbf{p}_{\mathrm{T}}^{\mathrm{miss}}$, with

$$m_{\mathrm{T}} = \sqrt{2p_{\mathrm{T}}E_{\mathrm{T}}^{\mathrm{miss}}(1-\cos(\Delta\phi))}. \tag{2}$$

The m_{T} of a W boson has a kinematic edge at the W mass, and signal events in SR3ℓ usually produce lepton-$E_{\mathrm{T}}^{\mathrm{miss}}$ pairings with a larger m_{T}. The minimum m_{T} of all lepton-$E_{\mathrm{T}}^{\mathrm{miss}}$ pairings for which the other two leptons form a SFOS pair, defined as $m_{\mathrm{T}}^{\mathrm{min}}$, is required to be $m_{\mathrm{T}}^{\mathrm{min}} > 125$ GeV in SR3ℓ. This definition allows WZ events to be rejected even if the incorrect SFOS pair was selected for the Z boson.

6 Background estimation and validation

Table 2: Selection criteria for the various signal, control, and validation regions used in the analysis. All regions require a pair of leptons with the same flavor and opposite sign of their electric charge whose invariant mass is between 81.2 GeV and 101.2 GeV. They additionally require a third lepton and a trilepton invariant mass above 90 GeV. The 2nd boson requirement indicates the presence of two additional jets or leptons consistent with a W, Z, or Higgs boson decay. The asterisk (*) in the SR4ℓ $E_{\mathrm{T}}^{\mathrm{miss}}$ requirement indicates that this selection is only considered for events with two pairs of same-flavor leptons. The $\Delta R(b_1, b_2)$ selection is only considered for events with at least two b-jets.

Region	N_{lep}	$E_{\mathrm{T}}^{\mathrm{miss}}$ [GeV]	$m_{\mathrm{T}}^{\mathrm{min}}$ [GeV]	2nd boson	2nd leptonic Z; $\lvert m_{\ell\ell,2} - m_Z \rvert$ [GeV]	$N_{\mathrm{b-jet}}$	$\Delta R(b_1, b_2)$	$m_{Z\ell}^{\mathrm{asym}}$
SRFR	≥4	-	-	Yes	veto; <20	-	<1.5	< 0.1
SR4ℓ	≥4	>80*	-	No	veto; <20	-	<1.5	-
CRZZ	=4	-	-	-	require; <5	-	<1.5	-
VRZZ	=4	-	-	-	require; [5,20]	-	<1.5	-
CR$t\bar{t}Z$	≥3	>40	-	-	veto; <20	≥2	>2.5	-
VR$t\bar{t}Z$	≥3	>40	-	-	veto; <20	≥2	[1.5,2.5]	-
SR3ℓ	=3	>150	>125	-	-	-	<1.5	-
CRWZ	=3	<80	[50,100]	-	-	-	<1.5	-
VR$E_{\mathrm{T}}^{\mathrm{miss}}$	=3	>80	<100	-	-	-	<1.5	-
VR$m_{\mathrm{T}}^{\mathrm{min}}$	=3	<80	>125	-	-	-	<1.5	-
CRFake	=3	<30	<30	-	-	-	<1.5	-
VRFake	=3	[30,80]	<30	-	-	-	<1.5	-

The MC samples described in Section 3 are used to predict the expected background yield from SM processes. To improve the accuracy of the MC prediction in the unique phase-space of this analysis and to constrain the systematic uncertainties, the MC predictions are normalized in control regions (CRs). Each CR is dedicated to the measurement of an important SM process and they are discussed in Section 6.1. A log-likelihood fit [100] is performed on all CRs and SRs simultaneously using the HistFitter package [101] to estimate the final post-fit background prediction and uncertainty. An additional CR is used for the data-driven *fake* estimation, discussed in Section 6.2, and is not included in the fit.

The CRs are developed to be kinematically similar to the SRs but with a small number of selections inverted, reducing any possible signal contamination and ensuring orthogonality between regions. Validation regions (VRs) between the CRs and SRs are developed to ensure the validity of the extrapolation of the yield normalization across the inverted selections and into the SRs. All regions are required to have at least three leptons and one SFOS pair with $m_{\ell\ell}$ within 10 GeV of the Z boson mass. The CRs and VRs are inclusive in $m_{Z\ell}$ as this variable is seen to be well-modeled by the MC simulation. A requirement of $m_{Z\ell} > 90$ GeV is made in all regions, corresponding to the lowest $m_{Z\ell}$ probed by the SRs. The selections for the various regions are discussed below and summarized in Table 2.

6.1 Primary backgrounds

The major SM backgrounds that are fitted in dedicated CRs are the WZ, ZZ, and $t\bar{t}Z$ processes. The yields of other SM processes are small and are therefore not normalized by the fit but taken directly from the MC prediction. These include the triboson, Higgs boson, and "Other" background categories, where Other almost completely consists of the tWZ, $t\bar{t}W$, and tZ processes.

The WZ process is dominant in the three-lepton SR3ℓ, and the CRWZ control region is developed by inverting the $E_{\mathrm{T}}^{\mathrm{miss}}$ requirement and selecting events with $m_{\mathrm{T}}^{\mathrm{min}}$ consistent with the presence of a W boson. This removes possible signal contamination from $\tilde{\chi}_1^{\pm}$ and $\tilde{\chi}_1^0$, which typically have a high $E_{\mathrm{T}}^{\mathrm{miss}}$ and $m_{\mathrm{T}}^{\mathrm{min}}$ in SR3ℓ due to one or more boosted neutrinos. Two VRs, VR$E_{\mathrm{T}}^{\mathrm{miss}}$ and VR$m_{\mathrm{T}}^{\mathrm{min}}$, are designed to test the validity of the WZ normalization in SR3ℓ using similar $E_{\mathrm{T}}^{\mathrm{miss}}$ and $m_{\mathrm{T}}^{\mathrm{min}}$ requirements, respectively. Good data-MC agreement is seen in both VRs, and the $E_{\mathrm{T}}^{\mathrm{miss}}$ and $m_{\mathrm{T}}^{\mathrm{min}}$ distributions are shown for CRWZ, VR$E_{\mathrm{T}}^{\mathrm{miss}}$, and VR$m_{\mathrm{T}}^{\mathrm{min}}$ in Figure 3.

The ZZ and $t\bar{t}Z$ processes are dominant in the four-lepton SR4ℓ and SRFR regions. A control region for the fully-leptonically decaying ZZ process, CRZZ, is developed by requiring the presence of a second SFOS pair of electrons or muons whose invariant mass $m_{\ell\ell,2}$ is within 5 GeV of the Z mass. The VRZZ validation region has a similar selection, but requires $m_{\ell\ell,2}$ to be between 5 and 20 GeV of the Z mass, falling naturally between the CRZZ requirement and the 20 GeV $m_{\ell\ell,2}$ veto of SR4ℓ and SRFR. The $m_{\ell\ell,2}$ distribution that includes both CRZZ and VRZZ is shown in Figure 3, and good agreement is seen between data and the post-fit background estimation. Events for which one Z decays to a pair of τ-leptons which both then subsequently decay leptonically are included in this validation region. Good modeling in the three-lepton regions is also expected for such ZZ events when only one τ-lepton decays leptonically, though this process is strongly suppressed by the $E_{\mathrm{T}}^{\mathrm{miss}}$ and $m_{\mathrm{T}}^{\mathrm{min}}$ requirements.

The control region CR$t\bar{t}Z$ targets the $t\bar{t}Z$ process in the SRs, for which the Z boson decays leptonically and one or both top quarks decay leptonically, and requires at least two b-jets in the event. The $\tilde{\chi}_1^{\pm}/\tilde{\chi}_1^0$ may also produce two b-jets through the decay of a Higgs boson, but they are less often produced back-to-back due to the boost of the Higgs boson decay product. Therefore, the b-jets in CR$t\bar{t}Z$ are required to be produced with $\Delta R(b_1, b_2) > 2.5$, while the SRs require events with at least two b-jets to satisfy $\Delta R(b_1, b_2) < 1.5$. A requirement of $E_{\mathrm{T}}^{\mathrm{miss}} > 40$ GeV is also imposed to reduce the contamination from the Z+jets process. To improve the statistics in CR$t\bar{t}Z$ the lepton multiplicity requirement is relaxed to $\mathrm{N}_\ell \geq 3$, allowing one top quark to decay fully hadronically. The presence or absence of a fourth lepton does not bias the other selections as the ratio of three-lepton to four-lepton events in the $t\bar{t}Z$ sample is well-modeled. The VR$t\bar{t}Z$ validation region is defined with the same selections but requiring $1.5 < \Delta R(b_1, b_2) < 2.5$, falling naturally between CR$t\bar{t}Z$ and the SRs. The $\Delta R(b_1, b_2)$ distribution for both CR$t\bar{t}Z$ and VR$t\bar{t}Z$ is shown in Figure 3.

To maintain orthogonality between the $t\bar{t}Z$ regions and the other CRs used in the fit, a requirement of $\Delta R(b_1, b_2) < 1.5$ is applied to all other analysis regions.

The $m_{Z\ell}$ distributions for the CRs and VRs are given in Figure 4. No significant shape disagreement is seen between data and MC simulation, validating the modeling of the backgrounds in $m_{Z\ell}$. The normalization in CRWZ, CRZZ, and CR$t\bar{t}Z$ is therefore performed inclusively in $m_{Z\ell}$ to improve the statistical precision.

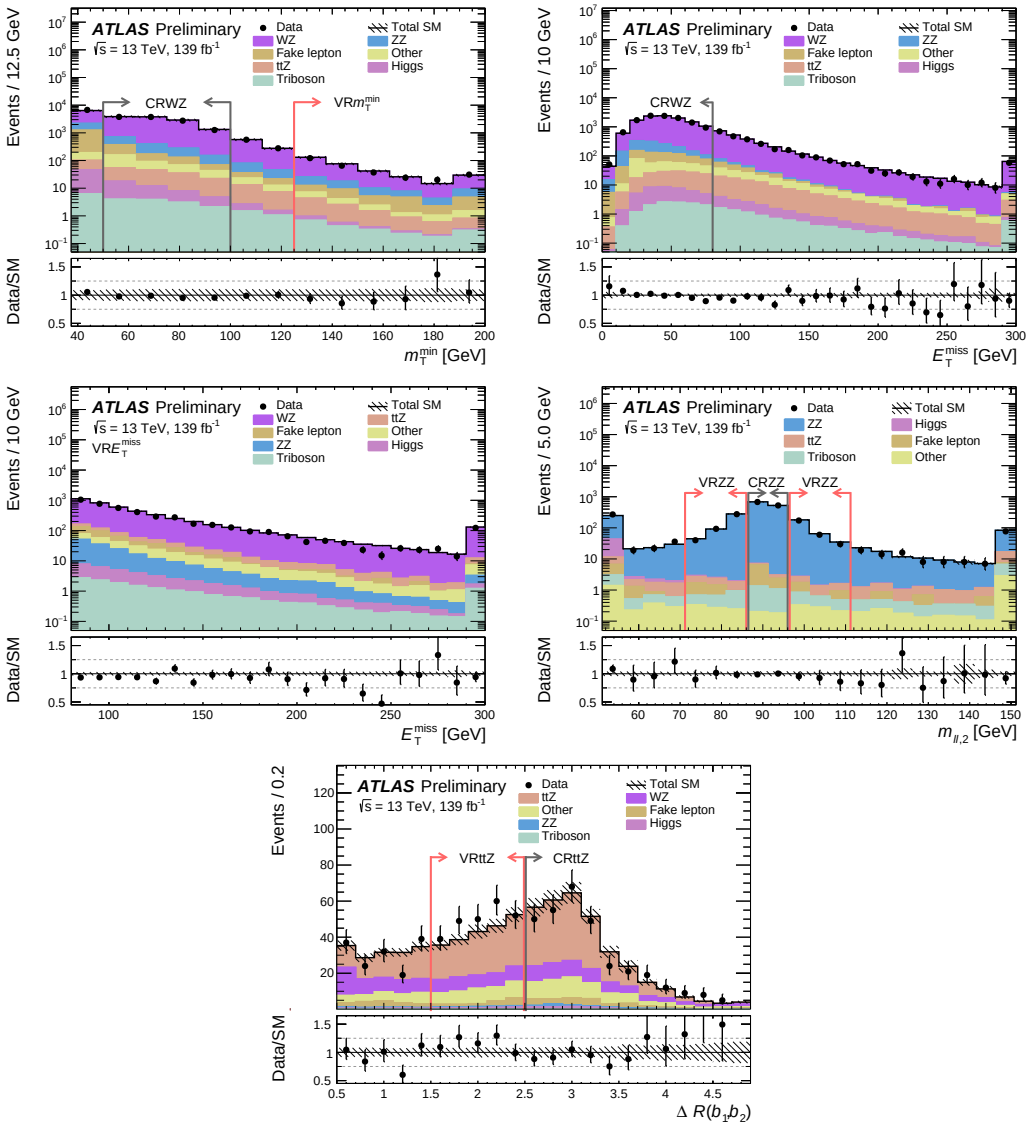

Figure 3: Distributions of the data and post-fit background in the CRs and VRs which are relevant in the extrapolation to the SRs, including (top left) $m_{\mathrm{T}}^{\mathrm{min}}$ in CRWZ and VR$m_{\mathrm{T}}^{\mathrm{min}}$, (top right) $E_{\mathrm{T}}^{\mathrm{miss}}$ in CRWZ, (middle left) $E_{\mathrm{T}}^{\mathrm{miss}}$ in VR$E_{\mathrm{T}}^{\mathrm{miss}}$, (middle right) $m_{\ell\ell,2}$ in CRZZ and VRZZ, and (bottom) $\Delta R(b_1, b_2)$ in CR$t\bar{t}Z$ and VR$t\bar{t}Z$. Black (red) arrows indicate the CR (VR) selection on the variable shown, with all other region selections applied. The first (last) bin includes underflow (overflow) events. The "Other" category mostly consists of tWZ, $t\bar{t}W$, and tZ processes. The bottom panel shows the ratio between the data and the post-fit background prediction. The hatched bands indicate the combined theoretical, experimental, and MC statistical uncertainties.

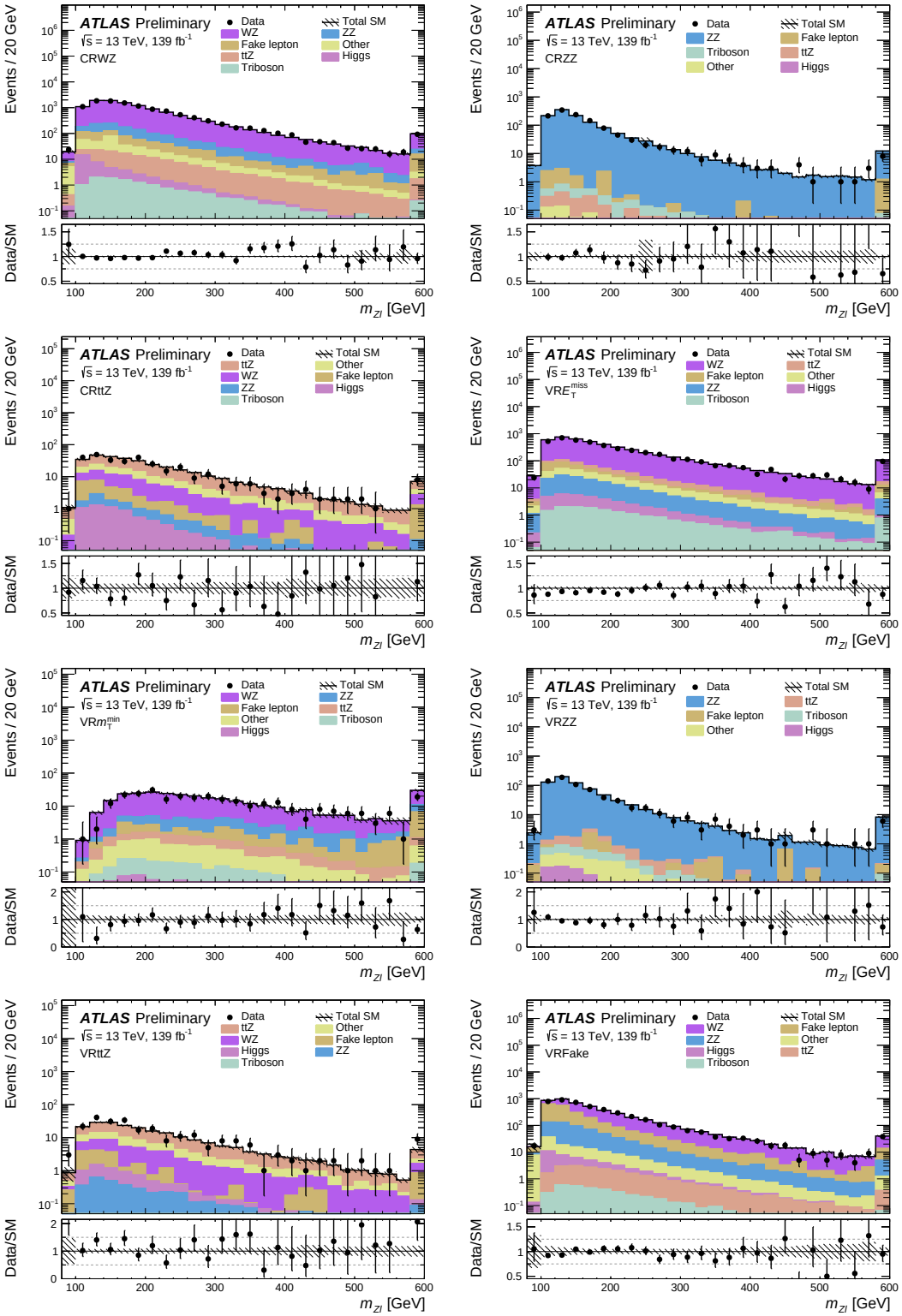

Figure 4: The $m_{Z\ell}$ distributions of the data and post-fit background in the CRWZ, CRZZ, CR$t\bar{t}Z$, VR$E_{\mathrm{T}}^{\mathrm{miss}}$, VR$m_{\mathrm{T}}^{\mathrm{min}}$, VR$ZZ$, VR$t\bar{t}Z$, and VRFake regions, respectively. The first (last) bin includes underflow (overflow) events. The "Other" category mostly consists of tWZ, $t\bar{t}W$, and tZ processes. The hatched bands indicate the combined theoretical, experimental, and MC statistical uncertainties. The bottom panel shows the ratio between the data and the post-fit background prediction.

The observed event yields in the CRs and VRs are compared with the background estimates and are shown in Figure 5. The CRs are shown with the pre-fit background estimation, and the bottom panel shows the relative disagreement which is subsequently reduced by the fit. The VRs are shown with the post-fit background estimation, and the bottom panel shows the significance of the disagreement when accounting for all uncertainties. Both the CRs and SRs are included in the fit, with the WZ, ZZ, and $t\bar{t}Z$ normalization factors primarily constrained by the CRs due to their high statistics and purity. The normalization factors of the background-only fit to the CRs and SRs are 1.03 ± 0.14 for the WZ process, 1.12 ± 0.08 for the ZZ process, and 1.05 ± 0.26 for the $t\bar{t}Z$ process.

The data agree well with the post-fit background estimates in all validation regions, giving confidence in the validity of the post-fit background estimation in the SRs. A slight overestimation of almost 2 σ is seen in VR$E_{\mathrm{T}}^{\mathrm{miss}}$, partially driven by the precision of the measurement. No features are seen in the comparison of data and the post-fit background estimation in the $m_{Z\ell}$ (Figure 4) or $E_{\mathrm{T}}^{\mathrm{miss}}$ (Figure 3) distributions of VR$E_{\mathrm{T}}^{\mathrm{miss}}$. A minor excess of data over the background estimation of 1.4 σ is seen in VR$t\bar{t}Z$, and good agreement is seen in the shape of the relevant $m_{Z\ell}$ (Figure 4) and $\Delta R(b_1, b_2)$ (Figure 3) distributions.

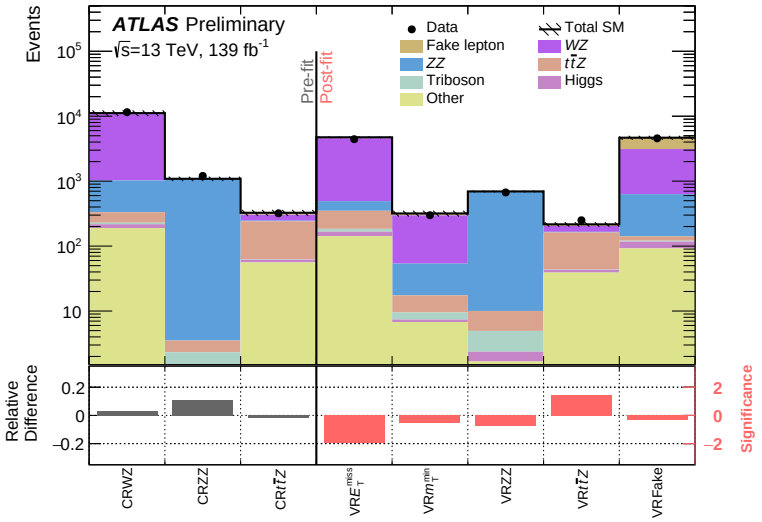

Figure 5: The observed data and the SM background expectation in the CRs (pre-fit) and VRs (post-fit). The "Other" category mostly consists of tWZ, $t\bar{t}W$, and tZ processes. The hatched bands indicate the combined theoretical, experimental, and MC statistical uncertainties. The bottom panel shows the fractional difference between the observed data and expected yields for the CRs and the significance of the difference for the VRs, computed following the profile likelihood method described in Ref. [102].

6.2 Backgrounds from *fake* leptons

Processes that include one or more *fake* leptons are estimated with the data-driven *fake*-factor method [103, 104], avoiding a reliance on MC simulation to model the prompt-lepton quality criteria of *fake* leptons. The modeling is also made difficult by the many sources of *fake*-lepton processes, each of which is kinematically different and whose relative contribution to the background estimate is dependent on the analysis phase-space. The most relevant sources for this analysis include the in-flight decays of heavy flavor hadrons (HF) and mis-identified light-flavor jets or in-flight decays of pions and kaons (LF). The *fake*

muons in this analysis are predominantly from HF sources while *fake* electrons are produced from both HF and LF sources, with their relative contribution varying from 2:1 to 1:5 depending upon the analysis region. The pair-production of two electrons from the conversion of a prompt photon (Conv) is also considered a *fake*-lepton process but has a minor contribution. In this analysis the relevant *fake* processes (and their sources) are Z+jets (LF, HF) and $t\bar{t}$ (HF) in the three-lepton regions and WZ (LF) and ZZ (LF, Conv) in the four-lepton regions, with SRFR also having a large contribution from $t\bar{t}Z$ (HF).

Pair-produced electrons are not considered as *fake* leptons if they are produced from the conversion of bremsstrahlung from a prompt electron, such as that from a leptonically-decaying Z boson. Events with such electrons are not targeted by the *fake*-factor method but are instead taken directly from MC simulation, which is considered to be sufficiently well-modeled for such processes. These events are included in the Other category and have a minor contribution in CRWZ and the *fake* measurement and validation regions, described below, and are negligible in all other regions.

A *fake* measurement region, CRFake, is designed to target the Z+jets process to provide a selection of events enhanced with *fake* leptons whose sources are representative of those expected in the SRs. Events are selected by requiring two signal leptons that form a SFOS pair and whose invariant mass is within 10 GeV of the Z boson mass. One of the two signal leptons is required to have fired a single-lepton trigger to ensure no selection bias from *fake* leptons. To enhance the Z+jets purity and reduce prompt contamination from the WZ process, CRFake requires $E_{\mathrm{T}}^{\mathrm{miss}} < 30$ GeV and $m_{\mathrm{T}} < 30$ GeV. A third, unpaired baseline lepton is also required in the event and is designated as the *fake* candidate. A requirement on the trilepton invariant mass of $m_{3\ell} > 105$ GeV reduces contamination from the $Z \to 4\ell$ process.

Events are split into two populations according to whether the *fake* candidate passes the nominal signal quality criteria (nom-ID) or fails at least one of the signal lepton identification, isolation, or impact parameter criteria (anti-ID). The expected contamination of prompt-lepton events from WZ and ZZ processes, as estimated from MC simulation, is subtracted from both populations so that they better represent the yields from *fake*-lepton sources. The *fake* factor is defined as the ratio of the yield of nom-ID to anti-ID events in CRFake and reflects the relative likelihood for a *fake* lepton that passes the baseline criteria to either pass or fail the signal lepton quality criteria. This ratio has a dependence on the *fake* lepton source but is fairly independent of the underlying physics process or any additional activity in the event. Therefore, in each analysis region the *fake* factor can be applied to a population of anti-ID events, defined with the same region selections but with one or more signal leptons replaced by anti-ID leptons, to predict the yield of *fake*-lepton events that have passed the selection requirements.

The *fake* factors are derived separately for electron and muon *fake* candidates and are parametrized as a function of $p_{\mathrm{T}}^{\mathrm{cone}}$, which better reflects the p_{T} of the underlying particle that has produced the *fake* lepton, such as a HF hadron. Additional parametrizations of the *fake* factor were considered, including lepton η, $E_{\mathrm{T}}^{\mathrm{miss}}$, and the b-jet multiplicity of the event, but a two-dimensional parametrization would significantly reduce the statistical precision of the *fake* factors. Alternative parametrizations are instead used to define a systematic uncertainty on the choice of $p_{\mathrm{T}}^{\mathrm{cone}}$. The statistical uncertainty of each *fake* factor is propagated to an uncertainty on the yield. An uncertainty on the prompt-lepton subtraction is performed by varying the subtracted yields of the WZ and ZZ MC simulations up and down by 5%, corresponding to their cross section uncertainties [105]. For any $m_{Z\ell}$ bin of a SR that does not have an anti-ID event, and therefore has a prediction of zero *fake*-lepton events, an uncertainty is applied corresponding to a yield of 0.32 *fake* events. This represents the largest *fake* estimation possible given a 1 σ upward fluctuation in the anti-ID event yield.

To validate the *fake* estimation, a dedicated validation region VRFake is developed closer to the SRs, using the same selections as CRFake but requiring $E_{\mathrm{T}}^{\mathrm{miss}} < 40$ GeV and $30 < m_{\mathrm{T}} < 50$ GeV. Good agreement is seen between data and the post-fit background estimation in VRFake, and for the other VRs, for all observables relevant for the *fake* factor, including the $m_{Z\ell}$ distributions shown in Figure 4. A conservative closure uncertainty of 23% (27%) is applied on the yield of events with electron (muon) *fake* candidates to cover the most discrepant $p_{\mathrm{T}}^{\mathrm{cone}}$ bin in VRFake.

The *fake* factor for electrons is sensitive to the relative composition of the *fake* sources, which primarily varies between LF and HF in the analysis regions. To derive an uncertainty on the *fake*-source composition, the MC *fake* factors are measured in MC simulation in CRFake for HF and LF sources separately. The inclusive MC *fake* factors are seen to be recovered by reweighting the HF and LF MC *fake* factors according to the CRFake composition. Therefore, a composition systematic uncertainty is derived in each analysis region by comparing the inclusive CRFake MC *fake* factors to those calculated from a reweighting of HF and LF MC *fake* factors, according to the composition of that region. The systematic uncertainty is derived using only MC simulation to provide clean sources of HF and LF *fake* electrons but is applied to the nominal data-driven *fake* factors, and is measured to be at most 53% for the electron *fake* factors in SR4ℓ.

7 Systematic uncertainties

Uncertainties in the expected signal and background yields account for the statistical uncertainties of the MC samples, the experimental systematic uncertainties in the detector measurements, and the theoretical systematic uncertainties of the MC simulation modeling. The uncertainties of the major backgrounds normalized in the CRs reflect the limited statistical precision of the CRs and the systematic uncertainties in the extrapolation to the signal regions, and an additional uncertainty on the normalization factor from the combined fit is included. The uncertainties related to the data-driven *fake* background estimation are described in detail in Section 6.2.

Systematic uncertainties are treated as Gaussian nuisance parameters in the likelihood while the statistical uncertainties of the MC samples are treated as Poisson nuisance parameters. Unless stated otherwise, each experimental uncertainty is treated as fully correlated across the analysis regions, while each theoretical uncertainty is derived as the relative yield between an analysis region and a control region and is treated as uncorrelated across analysis regions.

A summary of the background uncertainties is shown in Figure 6. Bin-to-bin fluctuations in the uncertainty on the *fake* background estimation reflect the low statistics in the anti-ID population and the conservative uncertainties applied when no anti-ID events are seen in the data. The effect of localized fluctuations in one SR is limited as all three SRs contribute to the overall sensitivity. A relative uncertainty of 2.2 is seen in the last $m_{Z\ell}$ bin of SRFR and is driven by an uncertainty of 2.0 on the fake estimation, reflecting the small post-fit background expectation of approximately 0.1 events.

Experimental uncertainties in the detector measurements reflect the accuracy of the kinematic measurements of jets, electrons, muons, and $E_{\mathrm{T}}^{\mathrm{miss}}$. Varying the scale or resolution of the energy or pt of objects within the uncertainties can cause the migration of events between $m_{Z\ell}$ bins or affect the inclusion of an event in an analysis region. The jet energy scale and resolution uncertainties [94, 106] are a large component of the experimental uncertainty and are derived as a function of jet p_{T} and η and account for the flavor and pileup dependencies of the detector energy measurement. Similar scale and resolution uncertainties are

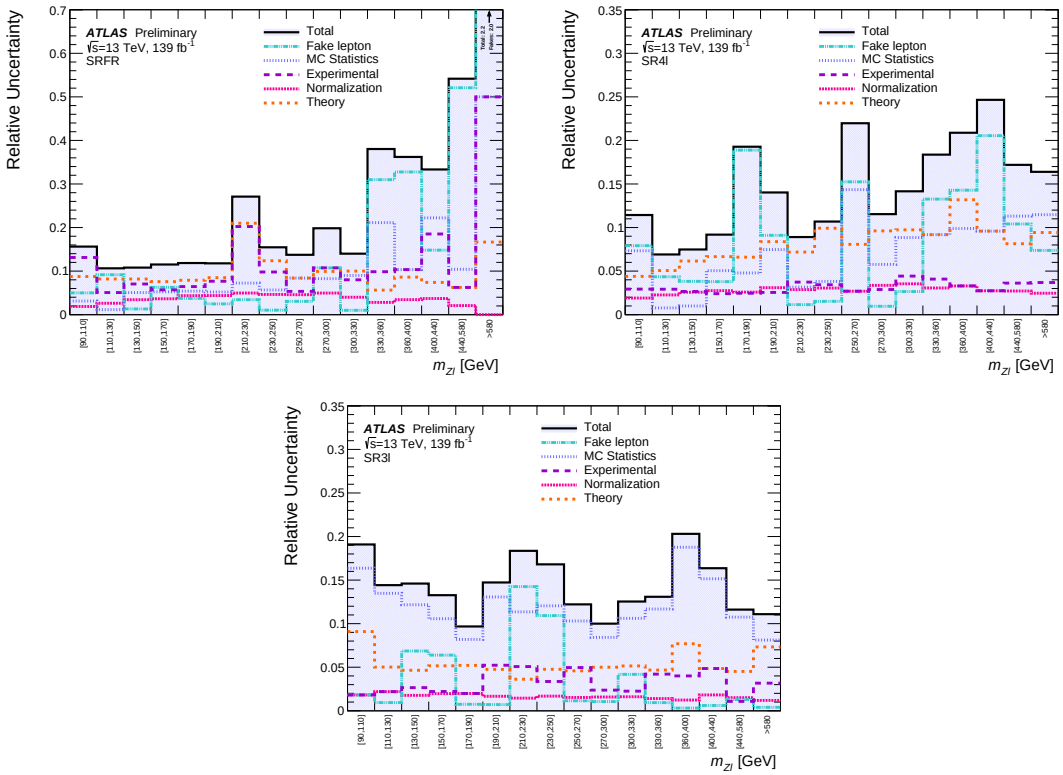

Figure 6: The relative uncertainties in the post-fit SM background prediction as a function of $m_{Z\ell}$ from the background-only fit for the (top left) SRFR, (top right) SR4ℓ, and (bottom) SR3ℓ regions. Sources of uncertainty are grouped into experimental, theoretical, and MC statistical categories. Separate categories are provided for the *fake* backgrounds and for the normalization procedure of the major WZ, ZZ, and $t\bar{t}Z$ backgrounds. The individual uncertainties can be correlated and do not necessarily add in quadrature to the total uncertainty.

included for electrons [89] and muons [90]. These per-object uncertainties are propagated through the $E_{\mathrm{T}}^{\mathrm{miss}}$ calculation, with additional uncertainties accounting for the scale and resolution of the $E_{\mathrm{T}}^{\mathrm{miss}}$ soft term [96].

Additional experimental uncertainties account for the mismodeling in MC simulation of observables related to the detection of leptons and jets. This includes the efficiency of the triggering, identification, reconstruction, and isolation requirements of electrons [89] and muons [90]. This also includes the identification and rejection of pileup jets by the jet vertex tagger [98] and the identification of b-jets by the flavor tagging algorithm [95]. The experimental uncertainty in the combined 2015–2018 integrated luminosity is 1.7% [107], obtained primarily using the luminosity measurements of the LUCID-2 detector [108].

Theoretical uncertainties in the shape of the major diboson, triboson, and $t\bar{t}Z$ backgrounds are derived using MC simulation with varied generator parameters. For the other minor backgrounds a conservative 20% uncertainty is assumed. Uncertainties due to the choice of the QCD renormalization and factorization scales [109] are assessed by varying the relevant generator parameters up and down by a factor of two around the nominal values, allowing for both independent and correlated variations of the two scales but prohibiting anti-correlated variations. Each QCD variation is kept separate and is treated as correlated across analysis regions. An uncertainty on the value of the strong coupling constant α_{S} of 1% is assessed by varying it

±0.001 in the generator parameters. Uncertainties related to the choice of PDF sets, CT14NNLO [110] or MMHT2014NNLO [111], are derived by taking the envelope of the variation in event yield of 100 propagated uncertainties.

Additional theoretical uncertainties are assessed in the major backgrounds related to assumptions made in the event generators and PS models, which can affect both the event kinematics and the cross section of the physics process. For the diboson backgrounds, the SHERPA parameters related to the PS matching scale, resummation scale, and recoil scheme are varied. For the $t\bar{t}Z$ background, the uncertainties in the hard-scatter and in the PS are derived through a comparison with the SHERPA and MADGRAPH5_AMC@NLO +HERWIG7 predictions, respectively. Additional uncertainties in the amount of initial-state radiation (ISR) of the $t\bar{t}Z$ background is assessed by varying the related generator parameters.

For the signal samples, theoretical uncertainties in the cross section are applied, ranging from 4.5% at 100 GeV to 16% at 1500 GeV. Uncertainties related to the QCD scale, PS matching scale, and amount of ISR are derived by varying the related generator parameters of the A14 tune [60].

8 Results

The data are compared to the post-fit background expectations described in Section 6 and no significant excess has been observed. The VRs, shown previously in Figure 5, demonstrate a good modeling of the post-fit background expectation in regions kinematically similar to the SRs and for a variety of observables, validating the background estimation technique. The observed and expected number of events in SRFR, SR4ℓ, and SR3ℓ are given in Table 3 inclusively in $m_{Z\ell}$ and for the inclusive, e, and μ direct-lepton flavor channels. The background expectation and uncertainty is further split into contributions from each category of SM processes. Separate fits are performed for each flavor channel, and the predicted yields in the e and μ channels may not necessarily add to the inclusive yield. The SRFR regions have flavor requirements on both direct leptons in an event, and the data yields in the e and μ channels do not add to the inclusive result.

The $m_{Z\ell}$ distributions in each SR, with binning corresponding to that used in the fit, are shown in Figure 7. The SRs show good agreement in the shape of the $m_{Z\ell}$ distribution between data and the SM expectation, with no significant localized excesses. Three example signals of mass 200, 500, and 800 GeV are included in these figures and peak strongly in their target $m_{Z\ell}$ bin for all three SRs, with the 800 GeV signal only visible in the last $m_{Z\ell}$ bin. Other observables in the SRs relevant for the extrapolation of the yield normalization are shown in Figure 8 and also demonstrate good agreement.

8.1 Model-independent limits on new physics in inclusive regions

Upper limits are set on the possible visible cross sections of generic beyond-the-SM (BSM) processes in each $m_{Z\ell}$ bin of each SR. These model-independent limits are derived at 95% confidence level (CL) using the CL_s prescription [112]. A profile log-likelihood fit is performed on the number of observed and expected events in the target $m_{Z\ell}$ bin of one SR and the three CRs, and a generic BSM process is assumed to contribute only to the target $m_{Z\ell}$ bin. In this way no assumption is made on the $\tilde{\chi}_1^{\pm}/\tilde{\chi}_1^0$ branching fractions or $m_{Z\ell}$ shape of the BSM process. No uncertainties are considered on the yield of the BSM process except for the luminosity uncertainty.

Table 3: The observed yields and post-fit background expectations in SRFR, SR4ℓ, and SR3ℓ, shown inclusively and when the direct lepton from a $\tilde{\chi}_1^{\pm}/\tilde{\chi}_1^0$ decay is required to be an electron or muon. The "Other" category mostly consists of tWZ, $t\bar{t}W$, and tZ processes. Uncertainties on the background expectation include combined statistical and systematic uncertainties. The individual uncertainties may be correlated and do not necessarily add in quadrature to equal the total background uncertainty.

Region	SRFR	SRFR$_e$	SRFR$_\mu$	SR4ℓ	SR4ℓ_e	SR4ℓ_μ
Observed yield	42	15	17	89	48	41
Expected background yield	39.3 ± 3.5	13.8 ± 2.1	15.7 ± 2.6	76 ± 5	36 ± 4	38.4 ± 2.9
WZ yield	–	–	–	–	–	–
ZZ yield	19.5 ± 2.8	7.2 ± 1.7	10.4 ± 2.5	21.0 ± 1.1	9.6 ± 0.7	11.2 ± 0.8
ttZ yield	12.3 ± 2.4	2.5 ± 0.7	3.0 ± 0.7	18 ± 5	9.1 ± 3.2	8.6 ± 1.6
triboson yield	1.3 ± 0.4	0.26 ± 0.09	0.32 ± 0.12	12.2 ± 2.4	5.7 ± 1.4	5.9 ± 1.5
Higgs yield	2.7 ± 0.5	0.73 ± 0.18	1.17 ± 0.25	11.2 ± 1.7	5.2 ± 1.0	5.5 ± 1.1
Other yield	2.2 ± 0.4	0.25 ± 0.17	0.39 ± 0.16	7.9 ± 1.3	4.0 ± 0.8	3.5 ± 0.8
$fake$ yield	1.3 ± 0.7	2.9 ± 1.5	0.5 ± 0.5	6.4 ± 2.1	2.1 ± 1.1	3.6 ± 1.7
Region	SR3ℓ	SR3ℓ_e	SR3ℓ_μ			
Observed yield	61	28	33			
Expected background yield	55.1 ± 3.0	27.6 ± 2.4	28.0 ± 2.3			
WZ yield	33.7 ± 2.1	16.6 ± 1.8	17.7 ± 1.9			
ZZ yield	0.93 ± 0.23	0.11 ± 0.04	0.79 ± 0.25			
ttZ yield	7.5 ± 1.6	4.1 ± 1.4	3.5 ± 0.7			
triboson yield	5.6 ± 1.2	2.7 ± 0.8	2.7 ± 0.7			
Higgs yield	0.51 ± 0.09	0.25 ± 0.06	0.23 ± 0.06			
Other yield	4.2 ± 0.7	2.0 ± 0.4	2.0 ± 0.5			
$fake$ yield	2.6 ± 1.1	1.9 ± 1.1	1.0 ± 0.8			

This procedure is repeated for each of the 16 $m_{Z\ell}$ bins in each of the three SRs, with only one SR bin considered for each fit. This differs from the fit previously discussed which is performed in the three CRs and the 48 $m_{Z\ell}$ bins simultaneously, and minor differences are seen compared to the significances shown in the bottom panel of Figure 7.

The model-independent limits are summarized in Table 4, which includes for each signal region:

- the number of observed events N_{obs},
- the number of expected SM events N_{exp} and the associated uncertainty from a fit to the CRs only,
- the observed limit on the visible cross section $\langle \epsilon\sigma \rangle_{\text{obs}}^{95}$ of the potential BSM process,
- the corresponding observed upper limit on the number of BSM events,
- the expected upper limit on the number of BSM events and the associated uncertainty,
- and the p-value (and associated significance Z) for the SM background alone to fluctuate to the number of observed events.

The definition of the observed limit on $\langle \epsilon\sigma \rangle^{95}_{\text{obs}}$ incorporates the cross section, acceptance, and selection efficiency of the generic BSM signal. No coherence is seen among the SRs in the significances for any $m_{Z\ell}$ bin, as would be expected in the presence of a resonance that contributes to all three SRs. The largest excess of data over the expected background is seen in SRFR for the $m_{Z\ell}$ region between 150 and 170 GeV, with an associated significance of 2.2 σ. This is consistent with expectations from statistical fluctuations of the SM background when considering 48 independent signal regions.

8.2 Mass limits on $B - L$ RPV pair-production

Hypothesis tests for the $B - L$ signal models are performed using the same CL_s prescription, with lower exclusion limits set on the $\tilde{\chi}_1^\pm/\tilde{\chi}_1^0$ masses for various scenarios of the $\tilde{\chi}_1^\pm/\tilde{\chi}_1^0$ branching fractions. A profile log-likelihood fit is performed simultaneously to the CRs and all $m_{Z\ell}$ bins of the three SRs, benefiting from the contribution of a signal model to a small number of $m_{Z\ell}$ bins coherently across SRFR, SR4ℓ, and SR3ℓ. The signal strength is represented by a single parameter of interest and coherently scales the signal yield across all regions.

The sensitivity to the signal models is dependent on the $\tilde{\chi}_1^\pm/\tilde{\chi}_1^0$ branching fractions to each lepton and boson type, and a scan is performed over various combinations. The contributions from the $\tilde{\chi}_1^\pm\tilde{\chi}_1^\mp$ and

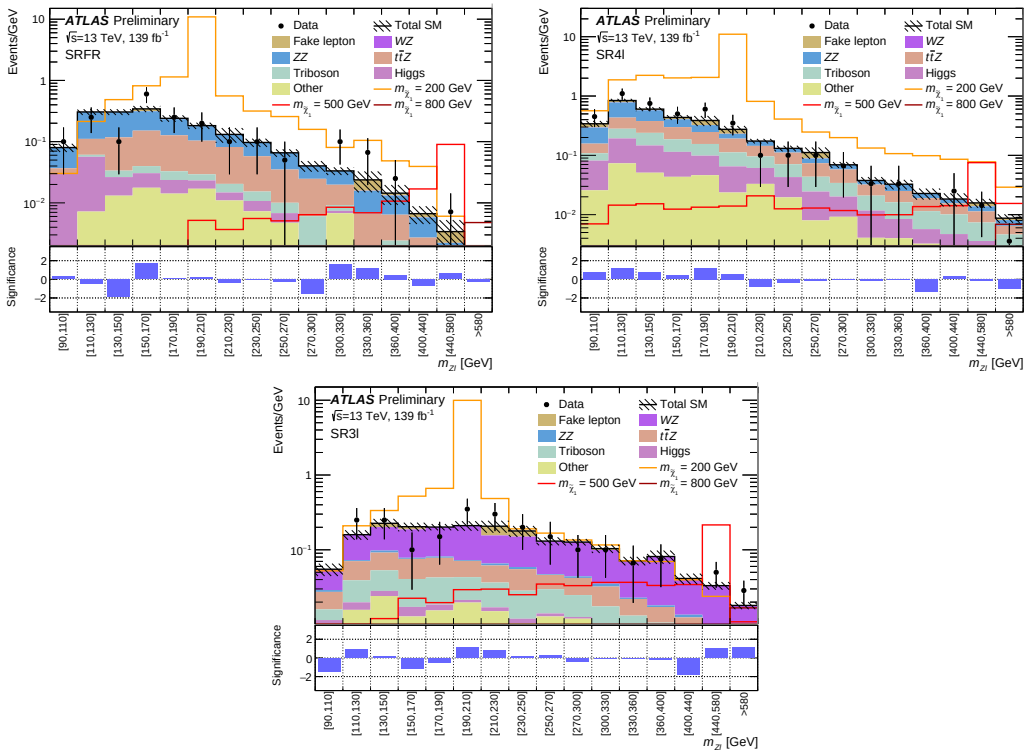

Figure 7: The observed data and post-fit SM background expectation as a function of $m_{Z\ell}$ in (top left) SRFR, (top right) SR4ℓ, and (bottom) SR3ℓ. The $m_{Z\ell}$ binning is the same as used in the fit and the yield is normalized to the bin width, with the last bin normalized using a width of 280 GeV. The "Other" category mostly consists of tWZ, $t\bar{t}W$, and tZ processes. The hatched bands indicate the combined theoretical, experimental, and MC statistical uncertainties. The bottom panel shows the significance of the differences between the observed data and expected yields, computed following the profile likelihood method described in Ref. [102].

$\tilde{\chi}_1^{\pm}\tilde{\chi}_1^0$ processes are treated together, and the $\tilde{\chi}_1^{\pm}/\tilde{\chi}_1^0$ branching fractions are treated as fully correlated. Four scenarios are considered for the $\tilde{\chi}_1^{\pm}/\tilde{\chi}_1^0$ branching fractions to leptons: the scenario with equal branching fractions to e, μ, and τ leptons and the three scenarios with 100% branching fractions to a single lepton type.

For each leptonic scenario, the $\tilde{\chi}_1^{\pm}/\tilde{\chi}_1^0$ branching fractions to W, Z, and Higgs bosons are scanned at 10% intervals. A 0% branching fraction to Z bosons is not explored and is replaced by a 1% branching fraction in the scans. No significant difference in sensitivity is seen for the relative $\tilde{\chi}_1^{\pm}/\tilde{\chi}_1^0$ branching fractions to W or Higgs bosons, with the sensitivity dominated by the branching fraction to Z bosons which produces the target trilepton resonances. The three SRs contribute roughly equally to the overall sensitivity of the search, with a minor increase in sensitivity to Higgs boson decays from SRFR offset by a similar increase in sensitivity to W boson decays from SR4ℓ.

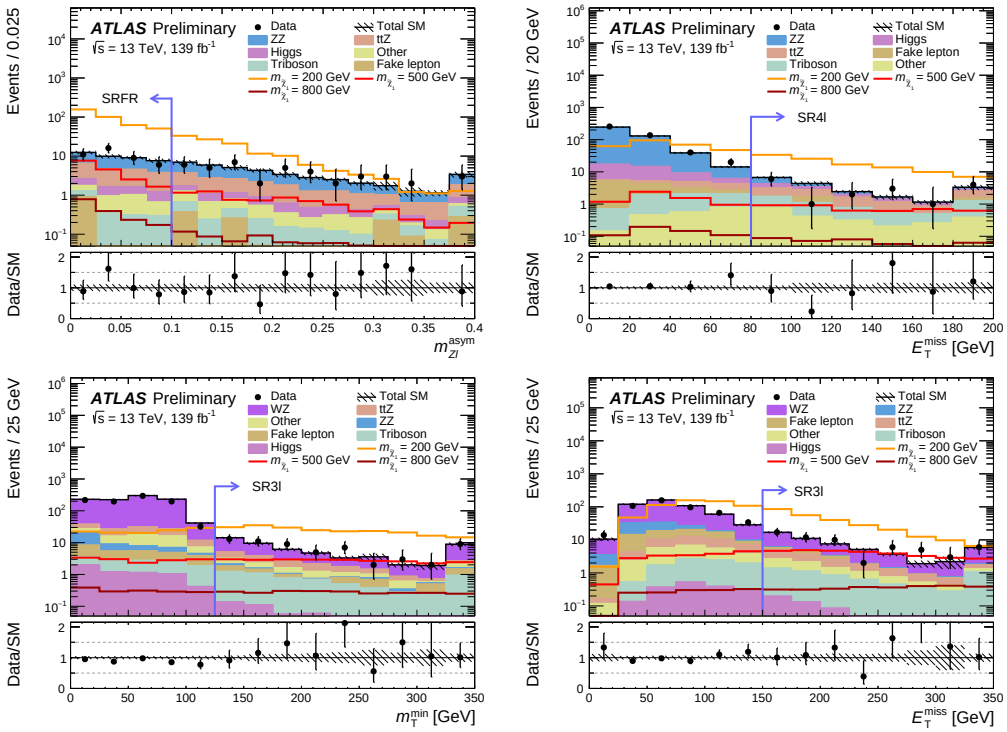

Figure 8: Example kinematic distributions in the signal regions showing the data and the post-fit background expectation, including (top left) $m_{Z\ell}^{\text{asym}}$ in SRFR, (top right) $E_{\text{T}}^{\text{miss}}$ in SR4ℓ, and (bottom left) $m_{\text{T}}^{\text{min}}$ and (bottom right) $E_{\text{T}}^{\text{miss}}$ in SR3ℓ. The fit uses all CR and SRs, and the distributions are shown inclusively in $m_{Z\ell}$. The full event selection for each of the corresponding regions is applied except for the variable shown, where the selection is indicated by a blue arrow. The first (last) bin includes underflow (overflow) events. The "Other" category mostly consists of tWZ, $t\bar{t}W$, and tZ processes. The hatched bands indicate the combined theoretical, experimental, and MC statistical uncertainties. The bottom panel shows the ratio between the data and the post-fit background prediction.

Table 4: Model-independent results where each row targets one $m_{Z\ell}$ bin of one SR and probes scenarios where a generic beyond-the-SM process is assumed to contribute only to that $m_{Z\ell}$ bin. The first two columns refer to the signal region and $m_{Z\ell}$ bin probed, while the third and fourth columns show the observed (N_{obs}) and expected (N_{exp}) event yields. The expected yields are obtained using a background-only fit of the CRs, and the errors include statistical and systematic uncertainties. The fifth and sixth columns show the observed 95% CL upper limit on the visible cross section ($\langle\epsilon\sigma\rangle^{95}_{\text{obs}}$) and on the number of signal events (S^{95}_{obs}), while the seventh column shows the expected 95% CL upper limit on the number of signal events (S^{95}_{exp}) with the associated 1 σ uncertainties. The last column provides the discovery p-value and significance (Z) of any excess of data above background expectation. Events for which the observed yield is less than the expected yield are capped at a p-value of 0.5.

Region	$m_{Z\ell}$ Range	N_{obs}	N_{exp}	$\langle\epsilon\sigma\rangle^{95}_{\text{obs}}$ [fb]	S^{95}_{obs}	S^{95}_{exp}	$p(s=0)$ (Z)
SRFR	[90,110]	2	1.6 ± 0.3	0.03	4.2	$4.0^{+1.7}_{-0.7}$	0.43 (0.2)
	[110,130]	5	5.9 ± 1.0	0.04	5.7	$6.4^{+2.5}_{-1.7}$	0.50 (0.0)
	[130,150]	2	6.0 ± 1.1	0.03	4.2	$6.2^{+2.3}_{-1.5}$	0.50 (0.0)
	[150,170]	12	6.1 ± 1.1	0.10	14.2	$7.9^{+2.7}_{-1.3}$	0.01 (2.2)
	[170,190]	5	4.5 ± 0.8	0.05	6.4	$5.6^{+2.5}_{-1.2}$	0.31 (0.5)
	[190,210]	4	3.4 ± 0.6	0.04	6.1	$5.2^{+2.0}_{-1.4}$	0.26 (0.7)
	[210,230]	2	2.6 ± 1.5	0.03	4.7	$4.9^{+1.9}_{-1.4}$	0.50 (0.0)
	[230,250]	2	1.8 ± 0.3	0.03	4.6	$4.0^{+1.7}_{-0.9}$	0.42 (0.2)
	[250,270]	1	1.2 ± 0.2	0.03	3.9	$3.7^{+1.6}_{-0.7}$	0.50 (0.0)
	[270,300]	0	1.2 ± 0.3	0.03	3.6	$3.7^{+1.5}_{-0.7}$	0.50 (0.0)
	[300,330]	3	0.9 ± 0.2	0.05	6.6	$4.2^{+0.7}_{-0.5}$	0.02 (2.1)
	[330,360]	2	0.5 ± 0.2	0.04	5.6	$3.5^{+0.8}_{-0.1}$	0.03 (1.9)
	[360,400]	1	0.5 ± 0.2	0.03	4.0	$3.4^{+0.8}_{-0.1}$	0.18 (0.9)
	[400,440]	0	0.3 ± 0.1	0.03	3.7	$3.1^{+0.8}_{-0.1}$	0.50 (0.0)
	[440,580]	1	0.3 ± 0.2	0.03	4.4	$3.3^{+0.9}_{-0.1}$	0.12 (1.2)
	>580	0	$0.1^{+0.2}_{-0.1}$	0.02	3.2	$3.0^{+0.1}_{-0.0}$	0.50 (0.0)
SR4ℓ	[90,110]	9	6.1 ± 0.9	0.07	9.7	$7.1^{+2.3}_{-1.1}$	0.14 (1.1)
	[110,130]	22	15.4 ± 1.3	0.12	16.0	$10.2^{+4.2}_{-2.1}$	0.05 (1.6)
	[130,150]	15	10.9 ± 0.9	0.09	12.7	$8.5^{+3.7}_{-1.2}$	0.09 (1.3)
	[150,170]	10	7.9 ± 0.9	0.07	9.9	$7.7^{+2.8}_{-1.4}$	0.18 (0.9)
	[170,190]	12	5.9 ± 0.6	0.10	14.3	$8.5^{+3.2}_{-0.8}$	0.02 (2.0)
	[190,210]	7	4.9 ± 0.9	0.06	8.4	$6.6^{+2.2}_{-1.2}$	0.16 (1.0)
	[210,230]	2	3.2 ± 0.3	0.03	4.3	$4.8^{+2.2}_{-1.4}$	0.50 (0.0)
	[250,270]	2	2.1 ± 0.6	0.03	4.5	$4.5^{+1.9}_{-1.0}$	0.50 (0.0)
	[270,300]	2	1.9 ± 0.2	0.03	4.9	$4.8^{+1.6}_{-1.2}$	0.48 (0.1)
	[300,330]	1	1.0 ± 0.2	0.03	4.7	$4.2^{+1.6}_{-0.9}$	0.50 (0.0)
	[330,360]	1	0.9 ± 0.2	0.03	3.9	$3.6^{+1.6}_{-0.5}$	0.30 (0.5)
	[360,400]	0	0.8 ± 0.2	0.03	3.6	$3.6^{+1.1}_{-0.5}$	0.50 (0.0)
	[400,440]	1	0.6 ± 0.2	0.03	4.2	$3.2^{+1.1}_{-0.2}$	0.17 (1.0)
	[440,580]	2	2.0 ± 0.4	0.03	4.7	$4.5^{+1.7}_{-1.2}$	0.50 (0.0)
	>580	1	2.3 ± 0.5	0.03	3.5	$4.5^{+1.7}_{-1.2}$	0.50 (0.0)
SR3ℓ	[90,110]	0	1.1 ± 0.2	0.02	3.0	$3.5^{+2.2}_{-0.5}$	0.50 (0.0)
	[110,130]	5	2.8 ± 0.6	0.06	7.8	$5.7^{+1.3}_{-1.1}$	0.09 (1.3)
	[130,150]	5	4.1 ± 0.8	0.05	6.8	$5.7^{+2.3}_{-1.2}$	0.27 (0.6)
	[150,170]	2	4.0 ± 0.7	0.03	3.8	$5.3^{+2.4}_{-1.5}$	0.50 (0.0)
	[170,190]	3	3.9 ± 0.5	0.04	4.9	$5.4^{+2.2}_{-1.7}$	0.50 (0.0)
	[190,210]	7	3.7 ± 0.8	0.07	9.1	$6.2^{+1.8}_{-1.6}$	0.12 (1.2)
	[210,230]	6	3.5 ± 0.9	0.06	8.9	$6.2^{+2.0}_{-1.1}$	0.09 (1.4)
	[230,250]	4	3.3 ± 0.7	0.04	6.0	$5.4^{+1.8}_{-1.2}$	0.29 (0.6)
	[250,270]	3	2.5 ± 0.4	0.04	5.4	$4.8^{+1.8}_{-1.3}$	0.37 (0.3)
	[270,300]	3	3.7 ± 0.5	0.04	5.1	$5.4^{+2.0}_{-1.7}$	0.50 (0.0)
	[300,330]	3	3.0 ± 0.5	0.04	5.0	$4.9^{+2.1}_{-1.2}$	0.50 (0.0)
	[330,360]	2	2.1 ± 0.4	0.03	4.7	$4.4^{+1.7}_{-1.1}$	0.50 (0.0)
	[360,400]	3	3.2 ± 0.9	0.04	5.4	$5.6^{+2.0}_{-1.8}$	0.50 (0.0)
	[400,440]	0	1.7 ± 0.3	0.02	3.0	$4.0^{+1.2}_{-0.6}$	0.50 (0.0)
	[440,580]	7	4.3 ± 0.7	0.06	8.7	$6.3^{+1.5}_{-1.6}$	0.11 (1.2)
	>580	8	4.6 ± 0.7	0.07	10.0	$6.6^{+2.3}_{-1.6}$	0.08 (1.4)

The expected and observed mass exclusion contours as a function of the $\tilde{\chi}_1^{\pm}/\tilde{\chi}_1^0$ branching fraction to Z bosons are shown in Figure 9 for each of the four lepton-flavor scenarios. The $\tilde{\chi}_1^{\pm}/\tilde{\chi}_1^0$ branching fractions to W and Higgs bosons are set to be equal here. Limits are set for signal masses above 100 GeV, and agreement within the uncertainties is seen between the observed and expected limits. The observed limit is slightly weaker than the expected limit due to the minor excesses seen at low $m_{Z\ell}$ in SR4ℓ and in some high $m_{Z\ell}$ bins in SRFR and SR3ℓ.

The observed mass exclusions are strongest when the $\tilde{\chi}_1^{\pm}/\tilde{\chi}_1^0$ branching fraction to Z bosons is largest, reaching 1050 GeV and 1000 GeV for the e and μ channels, respectively. The limit is slightly reduced to 950 GeV when no assumption is made on the flavor of the directly-produced lepton, and is weakest at 625 GeV when only $\tilde{\chi}_1^{\pm}/\tilde{\chi}_1^0$ decays to τ leptons are allowed. The observed mass limit becomes significantly reduced when the $\tilde{\chi}_1^{\pm}/\tilde{\chi}_1^0$ branching fraction to Z bosons falls below 20%, reaching 375 GeV in the μ channel and 300 GeV in the e channel when the branching fraction reaches 1%. No limits are set when requiring decays to τ-leptons for branching fractions to Z bosons below 12%.

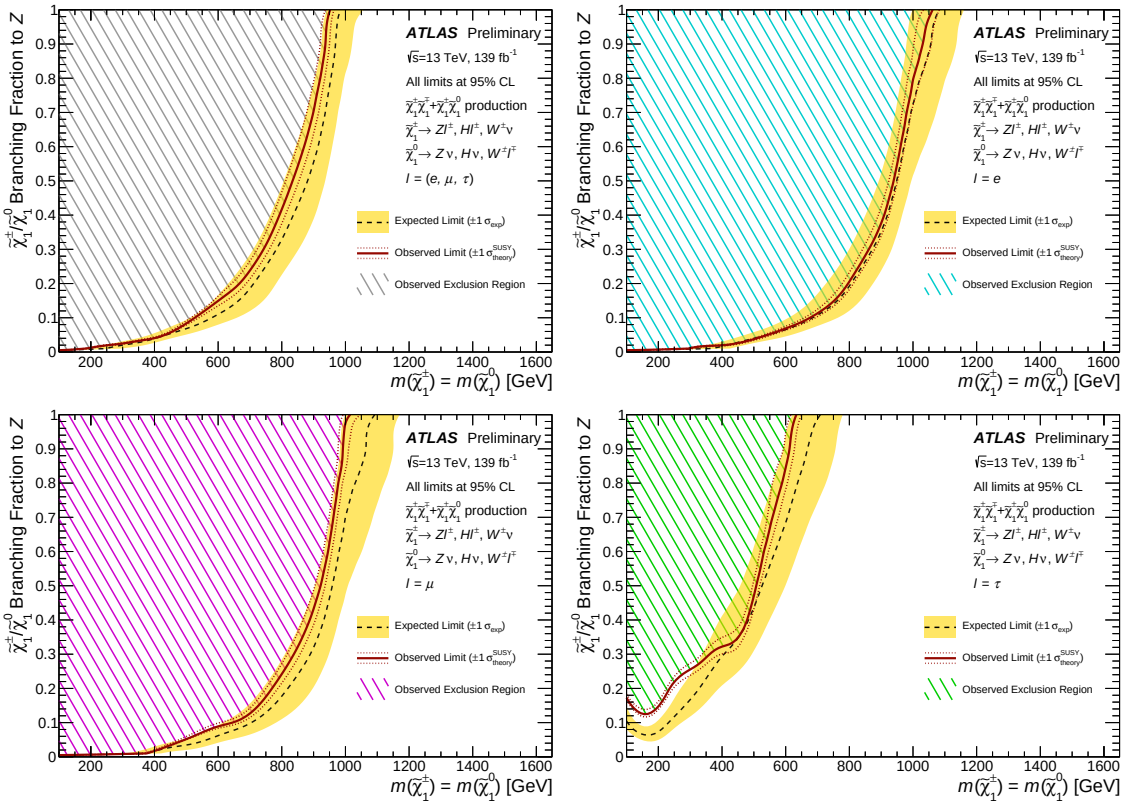

Figure 9: Exclusion curves for the simplified model of $\tilde{\chi}_1^{\pm}\tilde{\chi}_1^{\mp} + \tilde{\chi}_1^{\pm}\tilde{\chi}_1^0$ pair-production as a function of $\tilde{\chi}_1^{\pm}/\tilde{\chi}_1^0$ mass and branching fraction to Z bosons. Curves are derived separately when requiring that the charged-lepton decays of the $\tilde{\chi}_1^{\pm}/\tilde{\chi}_1^0$ are to (top left) any lepton with equal probability, (top right) an electron only, (bottom left) a muon only, or (bottom right) a τ lepton only. The expected 95% CL exclusion (dashed black line) is shown with $\pm 1\ \sigma_{\text{exp}}$ (yellow band) from systematic and statistical uncertainties on the expected yields. The observed 95% CL exclusion (solid red line) is shown with the $\pm 1\ \sigma^{\text{SUSY}}_{\text{theory}}$ (dotted red line) from signal cross section uncertainties on the signal models. The phase-space excluded by the search is shown in the shaded color. The sum of the $\tilde{\chi}_1^{\pm}/\tilde{\chi}_1^0$ branching fractions to W, Z, and Higgs bosons is unity for each point, and the branching fractions to W and Higgs bosons are chosen so as to be equal everywhere.

9 Conclusion

This paper presents a search for the production of wino-type $\tilde{\chi}_1^{\pm}\tilde{\chi}_1^{\mp}$ and $\tilde{\chi}_1^{\pm}\tilde{\chi}_1^{0}$ processes where each $\tilde{\chi}_1^{\pm}/\tilde{\chi}_1^{0}$ decays via an RPV coupling to a W, Z, or Higgs boson and a lepton. The dataset corresponds to an integrated luminosity of 139 fb^{-1} of proton–proton collision data produced at a center-of-mass energy of $\sqrt{s}$ = 13 TeV and collected by the ATLAS experiment between 2015 and 2018. This new search primarily targets the three-lepton decay of a $\tilde{\chi}_1^{\pm}$ and is the first ATLAS analysis using $\sqrt{s}$ = 13 TeV data to search for a mass resonance in the $m_{Z\ell}$ spectrum. Three signal regions are defined that target events with three or more leptons and missing transverse energy or with two fully-reconstructed $\tilde{\chi}_1^{\pm}/\tilde{\chi}_1^{0}$ decays. The observed event yields are found to be in agreement with Standard Model expectations, with no significant excess seen in the $m_{Z\ell}$ distributions of the signal regions.

Model-independent limits are set at a 95% confidence level for each $m_{Z\ell}$ bin in each signal region. The largest excess of data over the expectation in the 48 model-independent regions is found to be 2.2 σ. No trend is seen in the distribution of data excesses in $m_{Z\ell}$ bins between the three signal regions. Model-specific lower limits are also set on the $\tilde{\chi}_1^{\pm}/\tilde{\chi}_1^{0}$ masses for various decay branching fractions into electron, muon, or τ leptons and into W, Z, or Higgs bosons, probing sensitivity to the neutrino mass hierarchy and the MSSM parameters of the $B-L$ RPV theory. For scenarios with large $\tilde{\chi}_1^{\pm}/\tilde{\chi}_1^{0}$ branching fractions to Z bosons, lower limits on the $\tilde{\chi}_1^{\pm}/\tilde{\chi}_1^{0}$ masses are set at 625 GeV, 1000 GeV, and 1050 GeV for 100% branching fractions to τ leptons, muons, and electrons, respectively.

References

[1] Y. Golfand and E. Likhtman, *Extension of the Algebra of Poincare Group Generators and Violation of P Invariance*, JETP Lett. **13** (1971) 323, [Pisma Zh. Eksp. Teor. Fiz. **13** (1971) 452].

[2] D. Volkov and V. Akulov, *Is the neutrino a goldstone particle?*, Phys. Lett. B **46** (1973) 109.

[3] J. Wess and B. Zumino, *Supergauge transformations in four dimensions*, Nucl. Phys. B **70** (1974) 39.

[4] J. Wess and B. Zumino, *Supergauge invariant extension of quantum electrodynamics*, Nucl. Phys. B **78** (1974) 1.

[5] S. Ferrara and B. Zumino, *Supergauge invariant Yang-Mills theories*, Nucl. Phys. B **79** (1974) 413.

[6] A. Salam and J. Strathdee, *Super-symmetry and non-Abelian gauges*, Phys. Lett. B **51** (1974) 353.

[7] G. R. Farrar and P. Fayet, *Phenomenology of the production, decay, and detection of new hadronic states associated with supersymmetry*, Phys. Lett. B **76** (1978) 575.

[8] J. Ellis, J. Hagelin, D. V. Nanopoulos, K. A. Olive and M. Srednicki, *Supersymmetric relics from the big bang*, Nucl. Phys. B **238** (1984) 453.

[9] M. Pospelov, *Particle physics catalysis of thermal Big Bang Nucleosynthesis*, Phys. Rev. Lett. **98** (2007) 231301, arXiv: hep-ph/0605215.

[10] H. K. Dreiner, *An introduction to explicit R-parity violation*, Adv. Ser. Direct. High Energy Phys. **21** (2010) 565, arXiv: hep-ph/9707435.

[11] R. Barbier et al., *R-parity violating supersymmetry*, Phys. Rept. **420** (2005) 1, arXiv: hep-ph/0406039.

[12] P. Fayet, *Supersymmetry and Weak, Electromagnetic and Strong Interactions*, Phys. Lett. B **64** (1976) 159.

[13] P. Fayet, *Spontaneously Broken Supersymmetric Theories of Weak, Electromagnetic and Strong Interactions*, Phys. Lett. B **69** (1977) 489.

[14] V. Barger, P. Fileviez Perez and S. Spinner, *Minimal Gauged $U(1)_{B-L}$ Model with Spontaneous R-Parity Violation*, Phys. Rev. Lett. **102** (2009) 181802, arXiv: 0812.3661 [hep-ph].

[15] L. L. Everett, P. Fileviez Perez and S. Spinner, *The right side of TeV scale spontaneous R-Parity violation*, Phys. Rev. D **80** (2009) 055007, arXiv: 0906.4095 [hep-ph].

[16] V. Braun, Y.-H. He, B. A. Ovrut and T. Pantev, *A heterotic standard model*, Phys. Lett. B **618** (2005) 252, arXiv: hep-th/0501070.

[17] R. Deen, B. A. Ovrut and A. Purves, *The minimal SUSY $B - L$ model: simultaneous Wilson lines and string thresholds*, JHEP **07** (2016) 043, arXiv: 1604.08588 [hep-ph].

[18] P. Fileviez Perez and S. Spinner, *Spontaneous R-Parity breaking and left-right symmetry*, Phys. Lett. B **673** (2009) 251, arXiv: 0811.3424 [hep-ph].

[19] P. Fileviez Perez and S. Spinner, *The Minimal Theory for R-parity Violation at the LHC*, JHEP **04** (2012) 118, arXiv: 1201.5923 [hep-ph].

[20] P. Fileviez Perez and S. Spinner, *Supersymmetry at the LHC and the Theory of R-parity*, Phys. Lett. B **728** (2014) 489, arXiv: 1308.0524 [hep-ph].

[21] B. A. Ovrut, A. Purves, and S. Spinner, *A statistical analysis of the minimal SUSY $B - L$ theory*, Mod. Phys. Lett. A **30** (2015) 1550085, arXiv: 1412.6103 [hep-ph].

[22] B. A. Ovrut, A. Purves, and S. Spinner, *The minimal SUSY $B-L$ model: from the unification scale to the LHC*, JHEP **06** (2015) 182, arXiv: 1503.01473 [hep-ph].

[23] S. Dumitru, B. A. Ovrut and A. Purves, *The R-parity violating decays of charginos and neutralinos in the B-L MSSM*, JHEP **02** (2019) 124, arXiv: 1810.11035 [hep-ph].

[24] S. Dumitru, B. A. Ovrut and A. Purves, *R-parity violating decays of wino chargino and wino neutralino LSPs and NLSPs at the LHC*, JHEP **06** (2019) 100, arXiv: 1811.05581 [hep-ph].

[25] ATLAS Collaboration, *Search for electroweak production of supersymmetric particles in final states with two or three leptons at $\sqrt{s} = 13$ TeV with the ATLAS detector*, Eur. Phys. J. C **78** (2018) 995, arXiv: 1803.02762 [hep-ex].

[26] ATLAS Collaboration, *Search for direct production of charginos and neutralinos in events with three leptons and missing transverse momentum in $\sqrt{s} = 8$ TeV pp collisions with the ATLAS detector*, JHEP **04** (2014) 169, arXiv: 1402.7029 [hep-ex].

[27] CMS Collaboration, *Search for electroweak production of charginos and neutralinos in multilepton final states in proton–proton collisions at $\sqrt{s} = 13$ TeV*, JHEP **03** (2018) 166, arXiv: 1709.05406 [hep-ex].

[28] CMS Collaboration, *Combined search for electroweak production of charginos and neutralinos in proton–proton collisions at $\sqrt{s} = 13$ TeV*, JHEP **03** (2018) 160, arXiv: 1801.03957 [hep-ex].

[29] ATLAS Collaboration, *Search for type-III seesaw heavy leptons in pp collisions at $\sqrt{s} = 8$ TeV with the ATLAS Detector*, Phys. Rev. D **92** (2015) 032001, arXiv: 1506.01839 [hep-ex].

[30] ATLAS Collaboration, *Search for heavy lepton resonances decaying to a Z boson and a lepton in pp collisions at $\sqrt{s} = 8$ TeV with the ATLAS detector*, JHEP **09** (2015) 108, arXiv: 1506.01291 [hep-ex].

[31] CMS Collaboration, *Search for Evidence of the Type-III Seesaw Mechanism in Multilepton Final States in Proton–Proton Collisions at $\sqrt{s} = 13$ TeV*, Phys. Rev. Lett. **119** (2017) 221802, arXiv: 1708.07962 [hep-ex].

[32] ATLAS Collaboration, *Search for $B-L$ R-parity-violating top squarks in $\sqrt{s} = 13$ TeV pp collisions with the ATLAS experiment*, Phys. Rev. D **97** (2018) 032003, arXiv: 1710.05544 [hep-ex].

[33] Z. Marshall, B. A. Ovrut, A. Purves and S. Spinner, *LSP squark decays at the LHC and the neutrino mass hierarchy*, Phys. Rev. D **90** (2014) 015034, arXiv: 1402.5434 [hep-ph].

[34] ATLAS Collaboration, *The ATLAS Experiment at the CERN Large Hadron Collider*, JINST **3** (2008) S08003.

[35] ATLAS Collaboration, *ATLAS Insertable B-Layer Technical Design Report*, ATLAS-TDR-19, 2010, URL: https://cds.cern.ch/record/1291633, *ATLAS Insertable B-Layer Technical Design Report Addendum*, ATLAS-TDR-19-ADD-1, 2012, URL: https://cds.cern.ch/record/1451888.

[36] B. Abbott et al., *Production and integration of the ATLAS Insertable B-Layer*, JINST **13** (2018) T05008, arXiv: 1803.00844 [physics.ins-det].

[37] ATLAS Collaboration, *Performance of the ATLAS trigger system in 2015*, Eur. Phys. J. C **77** (2017) 317, arXiv: 1611.09661 [hep-ex].

[38] ATLAS Collaboration, *Performance of electron and photon triggers in ATLAS during LHC Run 2*, Eur. Phys. J. C **80** (2020) 47, arXiv: 1909.00761 [hep-ex].

[39] ATLAS Collaboration, *ATLAS data quality operations and performance for 2015–2018 data-taking*, JINST **15** (2020) P04003, arXiv: 1911.04632 [hep-ex].

[40] ATLAS Collaboration, *Multi-Boson Simulation for* 13 *TeV ATLAS Analyses*, ATL-PHYS-PUB-2017-005, 2017, URL: https://cds.cern.ch/record/2261933.

[41] ATLAS Collaboration, *ATLAS simulation of boson plus jets processes in Run 2*, ATL-PHYS-PUB-2017-006, 2017, URL: https://cds.cern.ch/record/2261937.

[42] E. Bothmann et al., *Event Generation with Sherpa 2.2*, (2019), arXiv: 1905.09127 [hep-ph].

[43] T. Gleisberg and S. Höche, *Comix, a new matrix element generator*, JHEP **12** (2008) 039, arXiv: 0808.3674 [hep-ph].

[44] S. Schumann and F. Krauss, *A parton shower algorithm based on Catani–Seymour dipole factorisation*, JHEP **03** (2008) 038, arXiv: 0709.1027 [hep-ph].

[45] S. Catani, F. Krauss, R. Kuhn and B. R. Webber, *QCD matrix elements + parton showers*, JHEP **11** (2001) 063, arXiv: hep-ph/0109231.

[46] S. Höche, F. Krauss, S. Schumann and F. Siegert, *QCD matrix elements and truncated showers*, JHEP **05** (2009) 053, arXiv: 0903.1219 [hep-ph].

[47] S. Höche, F. Krauss, M. Schönherr and F. Siegert, *A critical appraisal of NLO+PS matching methods*, JHEP **09** (2012) 049, arXiv: 1111.1220 [hep-ph].

[48] S. Höche, F. Krauss, M. Schönherr and F. Siegert, *QCD matrix elements + parton showers: The NLO case*, JHEP **04** (2013) 027, arXiv: 1207.5030 [hep-ph].

[49] F. Cascioli, P. Maierhofer and S. Pozzorini, *Scattering Amplitudes with Open Loops*, Phys. Rev. Lett. **108** (2012) 111601, arXiv: 1111.5206 [hep-ph].

[50] A. Denner, S. Dittmaier and L. Hofer, *Collier: a fortran-based Complex One-Loop LIbrary in Extended Regularizations*, Comput. Phys. Commun. **212** (2017) 220, arXiv: 1604.06792 [hep-ph].

[51] R. D. Ball et al., *Parton distributions for the LHC Run II*, JHEP **04** (2015) 040, arXiv: 1410.8849 [hep-ph].

[52] C. Anastasiou, L. J. Dixon, K. Melnikov and F. Petriello, *High precision QCD at hadron colliders: Electroweak gauge boson rapidity distributions at NNLO*, Phys. Rev. D **69** (2004) 094008, arXiv: hep-ph/0312266.

[53] S. Frixione et al., *A positive-weight next-to-leading-order Monte Carlo for heavy flavour hadroproduction*, JHEP **09** (2007) 126, arXiv: 0707.3088 [hep-ph].

[54] H. B. Hartanto, B. Jager, L. Reina and D. Wackeroth, *Higgs boson production in association with top quarks in the POWHEG BOX*, Phys. Rev. **D91** (2015) 094003, arXiv: 1501.04498 [hep-ph].

[55] E. Re, *Single-top Wt-channel production matched with parton showers using the POWHEG method*, Eur. Phys. J. C **71** (2011) 1547, arXiv: 1009.2450 [hep-ph].

[56] P. Nason, *A new method for combining NLO QCD with shower Monte Carlo algorithms*, JHEP **11** (2004) 040, arXiv: hep-ph/0409146.

[57] S. Frixione, P. Nason and C. Oleari, *Matching NLO QCD computations with parton shower simulations: the POWHEG method*, JHEP **11** (2007) 070, arXiv: 0709.2092 [hep-ph].

[58] S. Alioli, P. Nason, C. Oleari and E. Re, *A general framework for implementing NLO calculations in shower Monte Carlo programs: the POWHEG BOX*, JHEP **06** (2010) 043, arXiv: 1002.2581 [hep-ph].

[59] T. Sjöstrand et al., *An introduction to PYTHIA 8.2*, Comput. Phys. Commun. **191** (2015) 159, arXiv: 1410.3012 [hep-ph].

[60] ATLAS Collaboration, *ATLAS Pythia 8 tunes to 7 TeV data*, ATL-PHYS-PUB-2014-021, 2014, URL: https://cds.cern.ch/record/1966419.

[61] R. D. Ball et al., *Parton distributions with LHC data*, Nucl. Phys. B **867** (2013) 244, arXiv: 1207.1303 [hep-ph].

[62] ATLAS Collaboration, *Studies on top-quark Monte Carlo modelling for Top2016*, ATL-PHYS-PUB-2016-020, 2016, URL: https://cds.cern.ch/record/2216168.

[63] M. Czakon and A. Mitov, *Top++: A program for the calculation of the top-pair cross-section at hadron colliders*, Comput. Phys. Commun. **185** (2014) 2930, arXiv: 1112.5675 [hep-ph].

[64] M. Aliev et al., *HATHOR: HAdronic Top and Heavy quarks crOss section calculatoR*, Comput. Phys. Commun. **182** (2011) 1034, arXiv: 1007.1327 [hep-ph].

[65] P. Kant et al., *HatHor for single top-quark production: Updated predictions and uncertainty estimates for single top-quark production in hadronic collisions*, Comput. Phys. Commun. **191** (2015) 74, arXiv: 1406.4403 [hep-ph].

[66] S. Frixione, E. Laenen, P. Motylinski, B. R. Webber and C. D. White, *Single-top hadroproduction in association with a W boson*, JHEP **07** (2008) 029, arXiv: 0805.3067 [hep-ph].

[67] J. Alwall et al., *The automated computation of tree-level and next-to-leading order differential cross sections, and their matching to parton shower simulations*, JHEP **07** (2014) 079, arXiv: 1405.0301 [hep-ph].

[68] K. Hamilton, P. Nason, E. Re and G. Zanderighi, *NNLOPS simulation of Higgs boson production*, JHEP **10** (2013) 222, arXiv: 1309.0017 [hep-ph].

[69] ATLAS Collaboration, *Measurement of the Z/γ^* boson transverse momentum distribution in pp collisions at $\sqrt{s} = 7$ TeV with the ATLAS detector*, JHEP **09** (2014) 145, arXiv: 1406.3660 [hep-ex].

[70] J. Butterworth et al., *PDF4LHC recommendations for LHC Run II*, J. Phys. G **43** (2016) 023001, arXiv: 1510.03865 [hep-ph].

[71] U. Aglietti, R. Bonciani, G. Degrassi and A. Vicini, *Two-loop light fermion contribution to Higgs production and decays*, Phys. Lett. B **595** (2004) 432, arXiv: hep-ph/0404071.

[72] S. Actis, G. Passarino, C. Sturm and S. Uccirati, *NLO electroweak corrections to Higgs boson production at hadron colliders*, Phys. Lett. B **670** (2008) 12, arXiv: 0809.1301 [hep-ph].

[73] J. Pumplin et al., *New generation of parton distributions with uncertainties from global QCD analysis*, JHEP **07** (2002) 012, arXiv: hep-ph/0201195.

[74] M. Ciccolini, A. Denner and S. Dittmaier, *Strong and electroweak corrections to the production of Higgs + 2 jets via weak interactions at the Large Hadron Collider*, Phys. Rev. Lett. **99** (2007) 161803, arXiv: 0707.0381 [hep-ph].

[75] T. Han and S. Willenbrock, *QCD correction to the $pp \to WH$ and ZH total cross sections*, Phys. Lett. B **273** (1991) 167.

[76] O. Brein, A. Djouadi and R. Harlander, *NNLO QCD corrections to the Higgs-strahlung processes at hadron colliders*, Phys. Lett. B **579** (2004) 149, arXiv: hep-ph/0307206.

[77] M. L. Ciccolini, S. Dittmaier and M. Krämer, *Electroweak radiative corrections to associated WH and ZH production at hadron colliders*, Phys. Rev. D **68** (2003) 073003, arXiv: hep-ph/0306234.

[78] W. Beenakker et al., *The Production of Charginos/Neutralinos and Sleptons at Hadron Colliders*, Phys. Rev. Lett. **83** (1999) 3780, arXiv: hep-ph/9906298, Erratum: Phys. Rev. Lett. **100** (2008) 029901.

[79] J. Debove, B. Fuks and M. Klasen, *Threshold resummation for gaugino pair production at hadron colliders*, Nucl. Phys. B **842** (2011) 51, arXiv: 1005.2909 [hep-ph].

[80] B. Fuks, M. Klasen, D. R. Lamprea and M. Rothering, *Gaugino production in proton-proton collisions at a center-of-mass energy of* 8 *TeV*, JHEP **10** (2012) 081, arXiv: 1207.2159 [hep-ph].

[81] B. Fuks, M. Klasen, D. R. Lamprea and M. Rothering, *Precision predictions for electroweak superpartner production at hadron colliders with Resummino*, Eur. Phys. J. C **73** (2013) 2480, arXiv: 1304.0790 [hep-ph].

[82] J. Fiaschi and M. Klasen, *Neutralino-chargino pair production at NLO+NLL with resummation-improved parton density functions for LHC Run II*, Phys. Rev. D **98** (2018) 055014, arXiv: 1805.11322 [hep-ph].

[83] C. Borschensky et al., *Squark and gluino production cross sections in pp collisions at* $\sqrt{s} = 13, 14, 33$ *and* 100 *TeV*, Eur. Phys. J. C **74** (2014) 3174, arXiv: 1407.5066 [hep-ph].

[84] D. J. Lange, *The EvtGen particle decay simulation package*, Nucl. Instrum. Meth. A **462** (2001) 152.

[85] ATLAS Collaboration, *The ATLAS Simulation Infrastructure*, Eur. Phys. J. C **70** (2010) 823, arXiv: 1005.4568 [physics.ins-det].

[86] S. Agostinelli et al., *GEANT4 – a simulation toolkit*, Nucl. Instrum. Meth. A **506** (2003) 250.

[87] ATLAS Collaboration, *The Pythia 8 A3 tune description of ATLAS minimum bias and inelastic measurements incorporating the Donnachie–Landshoff diffractive model*, ATL-PHYS-PUB-2016-017, 2016, URL: https://cds.cern.ch/record/2206965.

[88] ATLAS Collaboration, *Vertex Reconstruction Performance of the ATLAS Detector at* $\sqrt{s} = 13$ *TeV*, ATL-PHYS-PUB-2015-026, 2015, URL: https://cds.cern.ch/record/2037717.

[89] ATLAS Collaboration, *Electron and photon performance measurements with the ATLAS detector using the 2015–2017 LHC proton–proton collision data*, JINST **14** (2019) P12006, arXiv: 1908.00005 [hep-ex].

[90] ATLAS Collaboration, *Muon reconstruction performance of the ATLAS detector in proton–proton collision data at* $\sqrt{s} = 13$ *TeV*, Eur. Phys. J. C **76** (2016) 292, arXiv: 1603.05598 [hep-ex].

[91] ATLAS Collaboration, *Topological cell clustering in the ATLAS calorimeters and its performance in LHC Run 1*, Eur. Phys. J. C **77** (2017) 490, arXiv: 1603.02934 [hep-ex].

[92] M. Cacciari, G. P. Salam and G. Soyez, *FastJet user manual*, Eur. Phys. J. C **72** (2012) 1896, arXiv: 1111.6097 [hep-ph].

[93] M. Cacciari, G. P. Salam and G. Soyez, *The anti-k_t jet clustering algorithm*, JHEP **04** (2008) 063, arXiv: 0802.1189 [hep-ph].

[94] ATLAS Collaboration, *Jet energy scale measurements and their systematic uncertainties in proton–proton collisions at* $\sqrt{s} = 13$ *TeV with the ATLAS detector*, Phys. Rev. D **96** (2017) 072002, arXiv: 1703.09665 [hep-ex].

[95] ATLAS Collaboration, *ATLAS b-jet identification performance and efficiency measurement with $t\bar{t}$ events in pp collisions at $\sqrt{s}$ = 13 TeV*, Eur. Phys. J. C **79** (2019) 970, arXiv: 1907.05120 [hep-ex].

[96] ATLAS Collaboration, *Performance of missing transverse momentum reconstruction with the ATLAS detector using proton–proton collisions at $\sqrt{s}$ = 13 TeV*, Eur. Phys. J. C **78** (2018) 903, arXiv: 1802.08168 [hep-ex].

[97] ATLAS Collaboration, *Selection of jets produced in 13 TeV proton–proton collisions with the ATLAS detector*, ATLAS-CONF-2015-029, 2015, URL: https://cds.cern.ch/record/2037702.

[98] ATLAS Collaboration, *Performance of pile-up mitigation techniques for jets in pp collisions at $\sqrt{s}$ = 8 TeV using the ATLAS detector*, Eur. Phys. J. C **76** (2016) 581, arXiv: 1510.03823 [hep-ex].

[99] ATLAS Collaboration, *Tagging and suppression of pileup jets with the ATLAS detector*, ATLAS-CONF-2014-018, 2014, URL: https://cds.cern.ch/record/1700870.

[100] G. Cowan, K. Cranmer, E. Gross and O. Vitells, *Asymptotic formulae for likelihood-based tests of new physics*, Eur. Phys. J. C **71** (2011) 1554, arXiv: 1007.1727 [physics.data-an], Erratum: Eur. Phys. J. C **73** (2013) 2501.

[101] M. Baak et al., *HistFitter software framework for statistical data analysis*, Eur. Phys. J. C **75** (2015) 153, arXiv: 1410.1280 [hep-ex].

[102] R. D. Cousins, J. T. Linnemann and J. Tucker, *Evaluation of three methods for calculating statistical significance when incorporating a systematic uncertainty into a test of the background-only hypothesis for a Poisson process*, Nucl. Instrum. Meth. A **595** (2008) 480, arXiv: physics/0702156 [physics.data-an].

[103] ATLAS Collaboration, *Measurement of the WW cross section in $\sqrt{s}$ = 7 TeV pp collisions with the ATLAS detector and limits on anomalous gauge couplings*, Phys. Lett. B **712** (2012) 289, arXiv: 1203.6232 [hep-ex].

[104] ATLAS Collaboration, *Prospects for Higgs boson searches using the $H \to WW^{(*)} \to \ell\nu\ell\nu$ decay mode with the ATLAS detector at 10 TeV*, ATL-PHYS-PUB-2010-005, 2010, URL: https://cds.cern.ch/record/1270568.

[105] ATLAS Collaboration, *Measurement of $W^{\pm}Z$ production cross sections and gauge boson polarisation in pp collisions at $\sqrt{s}$ = 13 TeV with the ATLAS detector*, ATLAS-CONF-2018-034, 2018, URL: https://cds.cern.ch/record/2630187.

[106] ATLAS Collaboration, *Jet energy resolution in proton–proton collisions at $\sqrt{s}$ = 7 TeV recorded in 2010 with the ATLAS detector*, Eur. Phys. J. C **73** (2013) 2306, arXiv: 1210.6210 [hep-ex].

[107] ATLAS Collaboration, *Luminosity determination in pp collisions at $\sqrt{s}$ = 13 TeV using the ATLAS detector at the LHC*, ATLAS-CONF-2019-021, 2019, URL: https://cds.cern.ch/record/2677054.

[108] G. Avoni et al., *The new LUCID-2 detector for luminosity measurement and monitoring in ATLAS*, JINST **13** (2018) P07017.

[109] E. Bothmann, M. Schönherr and S. Schumann, *Reweighting QCD matrix-element and parton-shower calculations*, Eur. Phys. J. C **76** (2016) 590, arXiv: 1606.08753 [hep-ph].

[110] S. Dulat et al., *New parton distribution functions from a global analysis of quantum chromodynamics*, Phys. Rev. D **93** (2016) 033006, arXiv: 1506.07443 [hep-ph].

[111] L. Harland-Lang, A. Martin, P. Motylinski and R. Thorne, *Parton distributions in the LHC era: MMHT 2014 PDFs*, Eur. Phys. J. C **75** (2015) 204, arXiv: 1412.3989 [hep-ph].

[112] A. L. Read, *Presentation of search results: the CL_S technique*, J. Phys. G **28** (2002) 2693.